The neuroanatomy of Eml1 knockout mice, a model of subcortical heterotopia

Stephan Collins, Ana Uzquiano, Mohammed Selloum, Olivia Wendling, Marion Gaborit, Maria Osipenko, Marie-Christine Birling, Binnaz Yalcin, Fiona Francis

To cite this version:

Stephan Collins, Ana Uzquiano, Mohammed Selloum, Olivia Wendling, Marion Gaborit, et al.. The neuroanatomy of Eml1 knockout mice, a model of subcortical heterotopia. Journal of Anatomy, 2019, Human Cortex Development, 235 (3), pp.637-650. 10.1111/joa.13013 . hal-02303443

HAL Id: hal-02303443
https://hal.sorbonne-universite.fr/hal-02303443v1

Submitted on 2 Oct 2019

HAL is a multi-disciplinary open access archive for the deposit and dissemination of scientific research documents, whether they are published or not. The documents may come from teaching and research institutions in France or abroad, or from public or private research centers.

L'archive ouverte pluridisciplinaire **HAL**, est destinée au dépôt et à la diffusion de documents scientifiques de niveau recherche, publiés ou non, émanant des établissements d'enseignement et de recherche français ou étrangers, des laboratoires publics ou privés.

The neuroanatomy of *Eml*1 knockout mice, a model of subcortical heterotopia

Stephan C. Collins[1-5]#, **Ana Uzquiano**[6-8]#, **Mohammed Selloum** [1, 2, 3, 4, 9], **Olivia Wendling** [1, 2, 3, 4, 9], **Marion Gaborit**[1-4], **Maria Ossipenko**[1-4], **Marie-Christine Birling** [1, 2, 3, 4, 9], **Binnaz Yalcin**[1-4]*, **Fiona Francis**[6-8]*

[1] Institut de Génétique et de Biologie Moléculaire et Cellulaire, Illkirch, France.

[2] Centre National de la Recherche Scientifique, UMR7104, Illkirch, France.

[3] Institut National de la Santé et de la Recherche Médicale, U964, Illkirch, France.

[4] Université de Strasbourg, Illkirch, France.

[5] Centre des Sciences du Goût et de l'Alimentation, Université de Bourgogne-Franche Comté, Dijon, France.

[6] INSERM UMR S-1270, Paris, France

[7] Sorbonne Université, UMR S-1270, F-75005 Paris, France

[8] Institut du Fer à Moulin, Paris, France

[9] CELPHEDIA, PHENOMIN, Institut Clinique de la Souris (ICS), 1 rue Laurent Fries, F-67404 Illkirch-Graffenstaden, France

# Contributed equally to this work

* To whom correspondence should be addressed

For Peer Review Only

Abstract

The cerebral cortex is a highly organized structure, responsible for advanced cognitive functions. Its development relies on a series of steps including neural progenitor cell proliferation, neuronal migration, axonal outgrowth and brain wiring. Disruption of these steps leads to cortical malformations, often associated with intellectual disability and epilepsy. We have generated a new resource to shed further light on subcortical heterotopia, a malformation characterized by abnormal neuronal position. We describe here the generation and characterization of a knockout (KO) mouse model for Eml1, a microtubule-associated protein showing mutations in human ribbon-like subcortical heterotopia. As previously reported for a spontaneous mouse mutant showing a mutation in *Eml*1, we observe severe cortical heterotopia in the KO. We also observe abnormal progenitor cells in early corticogenesis, likely to be the origin of the defects. *Eml*1 KO mice on the C57BL/6N genetic background also appear to present a wider phenotype than the original mouse mutant, showing additional brain anomalies, such as corpus callosum abnormalities. We compare the anatomy of male and female mice and also study heterozygote animals. This new resource will help unravel roles for Eml1 in brain development and tissue architecture, as well as the mechanisms leading to severe subcortical heterotopia.

Keywords: cortical malformations, heterotopia, mouse model of developmental disorders.

For Peer Review Only

Introduction

Cerebral cortical development relies on highly regulated processes of cell proliferation, neuronal migration, growth of axons and dendrites, as well as synaptogenesis and refined connectivity. Defects in these steps lead to cortical pathology, and severe malformations are associated with abnormal progenitor cells and / or defects in migrating neurons (Bizzotto and Francis, 2015; Stouffer et al. 2015; Romero et al. 2018).

Although human cortical malformations are rare disorders, their combined incidence is of more than 1% in the human population. 14% of epileptic patients are believed to present a neuronal migration disorder. This percentage rises to 40% when considering those patients with intractable epilepsy (Farrell et al. 1992, Meencke and Veigh, 1992, Guerrini et al. 2005). Subcortical heterotopia is a malformation characterized by the presence of masses of neurons beneath the normal cortex. It can be associated with a delay in somatic development, intellectual disability as well as epilepsy (Bahi-Buisson et al. 2013).

Patients with compound heterozygote or homozygote mutations in *EML*1 exhibit giant bilateral ribbon-like heterotopia, presenting large clusters of neurons that are aberrantly positioned within the white matter (Kielar et al. 2014; Shaheen et al. 2017, OMIM #600348). *EML*1-mutation patients can also present hydrocephalus, polymicrogyria and macrocrania (Kielar et al. 2014, Shaheen et al. 2017), and suffer from refractory epilepsy, intellectual disability, and/or psychomotor developmental delay (Kielar et al. 2014, Shaheen et al. 2017).

We previously studied *Heterotopic Cortex* (*HeCo*) mice, a spontaneously

For Peer Review Only

arisen mouse line exhibiting a retrotransposon insertion in the *Eml*1 gene (Croquelois et al. 2009; Kielar et al. 2014). These mice show bilateral heterotopia below the cortex in dorso-medial regions, associated with a susceptibility to epilepsy, as well as learning and memory deficits (Croquelois et al. 2009).

Eml1 is a microtubule-associated protein expressed in proliferative progenitor zones from early stages of corticogenesis (Bizzotto et al. 2017, Kielar et al. 2014). It binds to both microtubules and soluble tubulin (Richards et al., 2015) and contains an N terminal domain with a coiled coil motif, and a C terminal region with a tandem beta propeller structure. Although its function remains relatively unknown, Eml1 is important for progenitor distribution and function in the developing neocortex (Bizzotto et al. 2017, Kielar et al. 2014). Indeed, heterotopia formation in the *HeCo* mouse was shown to involve abnormal radial glial cell progenitors (RGs) in early-mid corticogenesis (Kielar et al. 2014; Bizzotto et al. 2017), which are the main neuronal progenitor cell in the developing cortex. They are characterized by the presence of an apical and a long basal process, the latter serving as guide for radially migrating neurons (Gotz and Huttner, 2005; Matsuzaki and Shitamukai, 2015; Uzquiano et al. 2018). Because of abnormal RG distribution and basal process morphology in *HeCo* mice, migration is perturbed throughout corticogenesis with upper layer neurons permanently arrested in the neocortical white matter (Kielar et al. 2014). Additionally, RGs were reported to show abnormal spindle orientation and mitotic spindle length, indicating a possible role for Eml1 in mitosis (Bizzotto et al. 2017, Kielar et al. 2014).

Although other subcortical heterotopia mouse models have arisen

For Peer Review Only

(Beattie et al. 2017, Cappello et al. 2012, Jossin et al. 2017, Liu et al. 2018), the *HeCo* mouse line represents a good disease model, mimicking human subcortical heterotopia, and showing mutations in a gene also mutated in human patients.

*Eml*1 gene expression was verified in the *HeCo* mouse mutant and full length transcripts were shown to be absent. The retrotransposon insertion occurs towards the end of the gene and certain chimeric transcripts were identified between *Eml*1 and the retrotransposon (Kielar et al. 2014). The absence of reliable antibodies against this protein made it difficult to verify if mutant Eml1 isoforms were produced, however loss-of-function due to severe disruption of the major scaffolding beta propeller domains is predicted (Richards et al. 2015). *HeCo* mice also arose on an unusual in-crossed NOR-CD1 congenic background. We had the possibility in this project of developing *Eml*1 knockout (KO) mice on the C57BL/6N genetic background (B6/N), as well as performing detailed and extensive neuroanatomical analyses. We show here that *Eml*1 KO mice resemble *HeCo* mice, faithfully revealing subcortical heterotopia, visible as early as embryonic day (E) 18.5. RG progenitor cells are perturbed at E13.5, similar to *HeCo*. Neuroanatomical measures in adult KO-B6N mice reveal a wider phenotype than observed in *HeCo*, which is not restricted to the neocortex. Males and females are both affected, with especially males showing a consistent heterotopia phenotype. This work hence characterizes a new *Eml*1 KO resource, as well as illustrating wide systematic neuroanatomical analyses in neurological mouse mutants.

For Peer Review Only

Materials and methods

Mouse line and ethical statement

All mouse experimental procedures were performed in agreement with the EC directive 2010/63/UE86/609/CEE for the care and use of laboratory animals and every effort was made to minimize the number of animals used and their suffering. The neuroanatomical pipeline was approved by the local animal care, use and ethic committee of the Institute of Genetics and of Molecular and Cellular Biology (IGBMC) under accreditation number 2012-139. Embryonic analyses were approved by the French MESR 00984.02 authorization with protocols followed and approved by local ethical committees (Charles Darwin committee (Paris, France). The light cycle was controlled as 12 h light and 12 h dark (lights on at 7 am) and the temperature was maintained at 23±1 °C.

For Peer Review Only

Creation of an *Eml*1 mouse KO line

The *Eml*1 mutant mouse line was established at the PHENOMIN MCI/ICS (Mouse Clinical Institute -*Institut Clinique de la Souris*-, Illkirch, France; http://www-mci.u-strasbg.fr), in the framework of funding from the French Rare Disease Foundation. The *Eml*1 mutant line was generated and analyzed on the mouse genetic background C57BL/6N (B6N). LoxP sites surrounding exon 8 were first introduced into a genomic DNA targeting construct (**Supp. Fig. 1**). This vector contained a Neo cassette encompassed by two FRT sites upstream of the second loxP site. This targeting construct was introduced by electroporation to allow homologous recombination in B6N embryonic stem cells. After G418 selection, targeted clones were identified by long-range PCR using external primers and further confirmed by Southern blot with an internal Neo probe as well as 5’ and 3’ external probes. Two positive ES clones were injected into B6N blastocysts. Resulting male chimeras were bred with wild type B6N females in order to obtain germline transmission. Selection cassettes were excised by crossing with a Rosa *Cre Flpase* deleter mouse line (Birling et al. 2012). Standard biochemical and metabolic tests were performed. Briefly, blood collection was performed for hematology and clinical chemistry assessments. Procedures are detailed in the following link (http://www.mousephenotype.org/impress).

For Peer Review Only

Genotyping

The following primers were used for genotyping (**Supp. Fig. 1**):

Position	Primers	Sequence
Ef	7964	CCCTGAGCTTCCTCATAACTTCAGC
Ef2	7965	CAGGTCTGTGGGCTCTGTAACAGG
Er	7966	CACCCACTGAAGAAATGACTGGCAG
Er2	7967	CTTGTTAAAGCGTCTGCAGTCTGTCTG
Lf	7962	GAAAACGTGCTTTGCTGTGTACATAGG
Lr	7963	CGCCACCCTTTTCTACAAGTCATTTTTG
Lxr	4724	CGAAGTTATCTGCAGGTCGACCTTAAG
Mqf	6	GAAGAACGAGATCAGCAGCCTCTGTTCC
Mqr	265	TGCTAAAGCGCATGCTCCAGACTGC

To distinguish the knockout allele, primer pairs Lf-Lr (245 bp, knock-out (KO); 165 bp, WT) and Ef-Er (414 bp, KO; 309 bp WT) were used.

Neuroanatomical studies

Neuroanatomical studies were carried out independently in WT and *Eml*1$^{-/-}$ male and female mice at 7 weeks of age. We aimed for n=5 per group for male and n=4 per group for female 7 week animals, although for some measures, statistics were not computed (comparisons involving less than 3 animals; see the Figure legends for more information). Also at postnatal day 13 (P13), we aimed for n=3 per group for male and females in comparisons (see Figure legends for exceptions), as described previously (Collins et al. 2018). Of note, experiments with *Eml*1$^{+/-}$ mice were performed with n=3-4 for both males and females (see Figure legends for exceptions). Concerning adults, the 4 females and the 5 males used for 7 week studies each came from 3 different litters. Concerning all other analyses, the mice used came from at least 2 different litters. Exceptions are het male 7 week analyses and WT male E18.5 analyses. In these two cases, the animals used came only from one litter.

In brief, adult mouse brain samples were fixed in 10% buffered formalin for exactly 48 hours. 166 brain parameters, made of area and length measurements, as well as cell level features and 31 co-variates, were taken blind to the genotype across one well-defined sagittal section (**Supp. Fig. 2A, 2B** and Supp. Table 1).

Similarly, neuroanatomical studies were carried out at E18.5 (n=3 per group for a total of six groups including male and female; wild type (WT), heterozygous (het) and homozygous (hom), for exceptions see below). In order to obtain the samples, het-het crosses were established thus allowing analyses of littermates. Mouse embryo head tissue samples were harvested and fixed in Bouin's fixative for exactly 48 hours followed by careful dissection of the brain and incubation in 70% ethanol before paraffin-embedded for sagittal sectioning. Brain sections were cut exactly in the plane of the closest image to the section defined as critical section at Lateral 0.60 mm of the right hemisphere numbered 9 (**Supp. Fig. 2, Supp. Fig. 3**). We failed brain sections that deviated more than 140 μm anterior or posterior to the critical section. When sectioning, great care was taken to avoid dorso-ventral and antero-posterior asymmetry. Sections were co-stained with cresyl violet and luxol blue as described previously

For Peer Review Only

(Collins et al. 2018). For E18.5 analyses, 46 brain parameters, concerning area and length measurements, were taken blind to the genotype across one sagittal section, as well as 31 co-variates (**Supp. Fig. 3B**). We have previously shown that our quantitative and ultra-standardized approach allowed us to detect many more features and more subtle phenotypes than previously published data (Mikhaleva et al. 2016).

For Peer Review Only

Immunohistochemistry analyses at P13

Immunohistochemistry analyses were performed in WT (n=3 for male and female), het (n=3 for male and 2 for female) and hom (n=3 for male and female) mice. Brains of P13 mice were fixed by immersion in ice-cold 4% (w/v) paraformaldehyde (PFA) in PBS during 24 hours, washed in 1 X PBS and embedded in paraffin. The sections from paraffin-embedded tissues were collected on glass slides and were treated with Tris-EDTA Buffer (10mM Tris Base, 1mM EDTA, 0.05% Tween 20, pH 9.0) at 94°C during 40 minutes (min.). The slides were cooled down at room temperature (RT) for 15 min. Blocking was performed during 1 hour at RT (1 X PBS with 5 % normal goat serum, 0.05 % tween 20). The primary antibody Tbr1 (Abcam, ab31940, 1:200) was incubated over-night (O/N) at 4°C. Then the secondary antibody Alexa 555 (Invitrogen, 1:500) was incubated for 1h at RT. The sections were then stained with DAPI (50 mg/ml) diluted in Tris-MWL 4-88 solution (Citifluor, EMS). Images were acquired with a TCS Leica SP5-II confocal microscope.

Immunohistochemistry analyses at early embryogenesis

Mouse embryos were obtained at E13.5 from timed-pregnant females. In order to obtain the samples, het-het crosses were established thus allowing analyses of littermates. For WT, *Eml*1 het and hom mice n=3-5 were analyzed from at least 3 different litters. Pregnant females were injected with 5-bromo-2'-deoxyuridine (BrdU, 99% Bioultra, Sigma-Aldrich Chimie Sarl, ref B9285, 50 µg per gram body weight) and sacrificed after 30 min. Mouse embryo head tissue samples were fixed by immersion O/N at 4 °C in 4 % w/v PFA in 0.1 M phosphate buffer, pH 7.4. Brains were dissected and extensively washed in 1 X PBS. Brains were cut in 70 µm thick coronal sections using a vibrating blade microtome (Leica VT1000 S), followed by immunohistochemistry. Blocking was performed for 1 h at RT with blocking solution (1X PBS with 10% Goat Serum and 0.5% Triton X-100) before incubation O/N at 4 °C with the following primary antibodies: Pax6 (BioLegend, Poly19013, 1:300) and N-Cadherin (Transduction Laboratories, C70320, 1:2000) (for other primary antibodies see below). After extensive washes, sections were incubated with secondary anti-mouse Alexa 488 or anti-rabbit Alexa 568 (Life Technologies, 1:1000) for 2 hours at RT. This was followed by 10 min. incubation in Hoechst (Thermo Fisher Scientific, 1:1000). After extensive washes, brain sections were mounted with Fluoromount G (Southern Biotechnology). For F-actin immunofluorescence, Alexa Fluor 568 Phalloidin (1:100, Life Technologies) was incubated in PBST 1% at RT after incubation with the secondary antibody. In order to perform immunohistochemistry combining the primary antibodies Ki67 (BD 556003, 1:200) and BrdU (BioRad, clone Bu20a, 1:1000) a modified protocol was applied. Antigen retrieval was performed by incubating the sections in sodium citrate 10 mM pH 6 at 95 °C for 20 min. and allowing them

For Peer Review Only

to cool before blocking. After blocking, incubation with the primary antibody (Ki67), secondary antibody and Hoechst, sections were fixed with PFA 8% w/v for 15 min. at RT (Palmer et al. 2000). Extensive washes with PBST-0.1% (1X PBS and 0.1% Triton X-100) were performed, followed by incubation of the sections in 2N hydrochloric acid for 30 min. at 37ºC. After extensive washes, the sections were incubated with the primary antibody (BrdU), secondary antibody, Hoechst, and then mounted with Fluoromount G as previously described.

In order to assess Pax6 positive (+) and Ki67+BrdU+ cell distribution, regions of interest (ROI) were selected from both hemispheres, spanning the whole cortical wall and with a width of 100 μm. Two ROIs were quantified per animal. The cortical wall was divided in six equally-sized bins, bin 1 and 6 corresponding to the most apical (apical ventricular zone) and basal (cortical plate) regions of the developing cortex, respectively (**Fig. 4A**, top row, right panel). Cells that were positive for the selected markers were quantified, and the percentage relative to the total number of positive cells was compared between the three genotypes (WT, het and hom), in each different bin. Images were acquired with a TCS Leica SP5-II confocal microscope.

For Peer Review Only

Statistical analyses

For adult and E18.5 analyses, data were analyzed using a two-tailed Student t-test of equal variance to determine whether a brain region was associated with the neuroanatomical defect or not. The level of significance was set at $p < 0.05$. Data are represented in a combined graph. Color-coded histograms according to the p-value show the percentage decreased (minus scale) or increased (plus scale) of measured brain regions as compared to the controls (0%). Data are also represented as box plots displaying the median with interquartile range. Box plots additionally indicate the number of animals specifically used for each parameter quantified. We only considered the exact same stereotaxic coordinates thus some animals could not be used to quantify certain specific parameters, explaining sometimes compromised sample size. Equally, due to the lower penetrance of the heterotopia phenotype in females (see below), a lower n number (2) was used when assessing heterotopia-specific characteristics in 7-week adults and E18.5 embryos. Related to heterotopia-specific characteristics, (area and height of HeCo and HoCo), data are represented as mean ± SEM.

For Peer Review Only

For E13.5 analyses, data were analyzed using the Kruskal-Wallis test with two factors (bin and genotype), followed by a Chi square test in order to compare between each genotype across the different bins. The level of significance was set at $p<0.05$. The median is represented and the error bars represent the minimum and maximum range. The analyses were performed with StatView and GraphPad Prism.

Results

Generation of an *Eml*1 KO mouse model

A knockout strategy was developed targeting *Eml*1 exon 8, with a view to drastically impacting the tandem beta propeller (TAPE) organization of the Eml1 protein (**Supp. Fig. 1A, 1B**). The TAPE structure is an important scaffolding domain representing the major part of the protein sequence (Richards et al. 2015). After homologous recombination, mice chimeras were generated incorporating the targeted allele (**Supp. Fig. 1C**) and crossed with a *Flp-Cre* deleter line (Birling et al. 2012). PCR genotyping confirmed the generation of the KO allele. Het mice were crossed to generate homozygotes, and the autosomal recessive nature of the heterotopia phenotype was confirmed (Croquelois et al. 2009).

For Peer Review Only

Postnatal lethality in a proportion of *Eml1* homozygous KO mice

Generating 235 animals with a het-by-het breeding scheme, at 3 weeks of age (weaning), mouse survival was estimated at 79 % and 185 animals were genotyped. We obtained 51% het, 29% WT and 20% hom, suggesting a possible lethality of a proportion of *Eml*1 homozygous mice (25 % expected). Of 19 homozygote juvenile/adult females, 7 were sacrificed for dissections or other reasons e.g. age (between 28-44 weeks). The remaining 12 (63.1 %) died earlier at an average age of 11 weeks (range 7-25 weeks), with at least 3 mice suffering from hydrocephalus. Of 16 homozygote juvenile/adult females, 6 were sacrificed for dissections or other reasons e.g. age (between 20-28 weeks). The remaining 10 (62.5 %) died earlier at an average age of 9.4 weeks (range 4-26 weeks), with at least 2 mice known to suffer from hydrocephalus. Thus, male and female *Eml*1 KO mice seemed relatively equally affected by the lethality, and severe hydrocephalus was noted in certain individuals (see also below). A small proportion of *Eml*1 het mice (10 %) also died between 5-16 weeks of age. Blood haematology and blood chemistry analyses at 7 weeks of age showed no major differences between WT and KO mice (data not shown).

Identification of defects in *Eml*1 KO mice including double cortex, corpus callosum agenesis, abnormal hippocampus and hydrocephalus

We examined the brain anatomy of *Eml*1 homozygous mice at 7 weeks of age, both in males and females, using a platform for the parasagittal histo-phenotyping of the mouse brain (Collins et al. 2018). Slide scans down to cell level resolution (**Supp. Fig. 2A**) were used to quantify 40 brain parameters across 22 distinct brain structures (**Supp. Table 1** and **Supp. Fig. 2B**) from a single sagittal brain section at Lateral +0.60 mm. This quantification was blind to the genotype. To minimize environmental and genetic variation, mice were analyzed according to their gender, aged exactly 7 weeks, and bred on the same genetic background (B6N).

Severe brain anomalies were found and are summarized in **Fig. 1A**. As previously reported in an *Eml*1-spontaneous mouse mutant (Croquelois et al. 2009, Kielar et al. 2014), underneath a homotopic thinner cortex a massive heterotopia surrounded by fiber tracts formed a double cortex (**Fig. 1B**). Considering analyses testing at least 3 mice per genotype, other neuroanatomical defects included cell dispersion in the CA3 region of the hippocampus (**Fig. 1B**), an enlarged area of the hippocampal pyramidal cell layer (+122%, *P*=0.01 for male compared to +45%, *P*=0.37 for female *Eml*1$^{-/-}$ mice; **Fig. 1B**), together with increased area of the dorsal subiculum (+170%, *P*=0.006 for male compared to +89%, *P*=0.12 for female *Eml*1$^{-/-}$ mice; **Fig. 1B**). The commissures were also affected showing corpus callosum agenesis (5/5 affected for *Eml*1$^{-/-}$ males compared to 2/4 affected for *Eml*1$^{-/-}$ females), a smaller area of the anterior commissure (-27%, *P*=0.015 for male *Eml*1$^{-/-}$ mice),

For Peer Review Only

and an enlargement of the lateral ventricles (+266%, *P*=0.046 for male and +136%, *P*=0.12 for female *Eml*1$^{-/-}$ mice). Some variability in female phenotypes may explain why the significance threshold of 0.05 was never reached despite the large effect size (**Fig. 1A**). It is however important to note that males and females shared a very similar phenotypic profile.

In addition, we also examined the brain anatomy of male *Eml*1 het mice at 7 weeks of age using the same approach. We were unable to detect any major differences between the brain anatomy of *Eml*1 het mice when compared to their matched controls (**Fig. 1C**), although a decrease of 8% of the size of the anterior commissure was observed after the analysis of n=2 mice for each genotype.

The cortical heterotopia is associated with corpus callosum agenesis and hippocampal defects but not with hydrocephalus

In two *Eml*1$^{-/-}$ female mice (out of four assessed), we did not see the subcortical heterotopia nor the corpus callosum agenesis and hippocampal-related phenotypes despite the presence of the hydrocephalus. Similarly, in one *Eml*1$^{-/-}$ male mice (out of five tested), the heterotopia, corpus callosum agenesis and hippocampal-related phenotypes segregated but without the enlarged ventricles. Together, these results suggest that the underlying biological mechanisms leading to heterotopia, corpus callosum agenesis and hippocampal defects might be shared and may be independent of the enlarged ventricle phenotype.

To further characterize the heterotopia phenotype, we quantified seven additional parameters (illustrated in **Supp. Fig. 2C**). We analyzed the normal

For Peer Review Only

cortex in WT mice and its corresponding homotopic cortex (HoCo) as well as the heterotopic cortex (HeCo) in *Eml*1 hom mice that exhibited the heterotopia phenotype. The area and the height of the homotopic cortices were reduced in male *Eml*1 hom mice (for area: -34.8%, *P*=0.0078, for height: -58.9%, *P*=3.19E-05, **Fig. 1D**), when compared to the normal total cortex (**Fig. 1D**). Analyzing n=2 female mice with heterotopia revealed potentially similar results (for area: -37.4%; for height: -55.9% compared to WT, Fig. 1D). The combined height of HeCo and HoCo remained the same size in male and female *Eml*1 hom mice, however their combined area appeared moderately smaller in n=2 female *Eml*1 hom mice (-17.6%, **Fig. 1D**).

For Peer Review Only

The hydrocephalus phenotype is visible at postnatal day 13 (P13)

Next, we assessed neuroanatomical defects in *Eml*1 hom mice at P13, both in males and females using the same platform as the one used for the parasagittal histo-phenotyping of the adult mouse brain (**Supp. Fig. 2B**). In line with the adult data, when comparing at least 3 mice for each condition, similar neuroanatomical defects were also seen at P13 in both male and female KOs (**Fig. 2A**): a massive heterotopia surrounded by fiber tracts and cell dispersion in the CA3 layer of the hippocampus. An enlarged size of the ventricles was observed in male KOs (**Fig. 2B**), and a similar tendency when analyzing n=2 females. An increased area of the dorsal subiculum was also observed in n=3 females, with a similar tendency in n=2 males. In one *Eml*$1^{-/-}$ female mice, the heterotopia, corpus callosum agenesis and hippocampal-related phenotypes did not segregate with enlarged ventricles, further suggesting that these neuroanatomical anomalies are likely to be unrelated. We also analyzed the normal cortex in WT mice and its corresponding homotopic cortex (HoCo) as well as the heterotopic cortex (HeCo) in *Eml*$1^{-/-}$ mice. In a manner similar to adult mice, there was a tendency towards a reduced area and the height of the homotopic cortices both in male and female *Eml*$1^{-/-}$ mice when compared to the normal total cortex (**Fig. 2C**). There was also a tendency towards a decreased area of the combined area of HeCo and HoCo both in male and female mice, however their combined height seemed to be enlarged when compared to matched controls (**Fig. 2C**).

In order to shed further light on the identity of the cells composing the heterotopia, we performed immunostainings for Tbr1 in male and female WT, het and hom (all n=3) mice (**Fig. 2D**). Although Tbr1 is expressed in diverse populations of cortical neurons, it is highly expressed in deep layers of the CxP (Molyenaux et al. 2007), serving as a marker of the latter. We observed that highly-expressing Tbr1+ neurons are localized in deep layers of the WT and het cortices, as well as in the normotopic cortex of *Eml*1 KO mice. As previously reported for the *Eml*1-spontaneous mouse mutant (Croquelois et al. 2009), Tbr1+ neurons are mostly absent from the heterotopia. However, we observed some sparse cells positive for Tbr1, suggesting that even if most of the heterotopia is composed of upper-layer neurons, a very small population of deep-layer neurons are also arrested beneath the normotopic cortex.

For Peer Review Only

Embryonic origins of the brain anomalies: analysis at E18.5

The time scale of neuroanatomical defects was further investigated through a similar morphological screen at E18.5. Coherent with the adult brain screen, we assessed 39 brain parameters (listed in **Supp. Table 2** and schematized in

Supp. Fig. 3B) distributed across 11 distinct brain regions of the developing brain (cortical layers, hippocampus, thalamus, basal ganglia, fiber tracts, cerebellum, pons, ventricle, forebrain and midbrain).

In line with the adult and P13 data, major neuroanatomical defects were identified at E18.5 in both male and female KO mice (summarized in **Fig. 3A**). Most of the assessed parameters pertaining to the cortical wall (Cxne, neuroepithelial ventricular zone; SubVCx, subventricular zone; ICx, intermediate zone; higher CxP, superficial cortical plate) appeared decreased in size when compared to matched WT brains. For example, the superficial CP was smaller (-64.8%, *P*=0.0009 for male and -62.0%, *P*=0.0013 for female *Eml*$1^{-/-}$ mice, **Fig. 3A**). The deep cortical plate (CxP) area also showed a similar reduction by 79.4% (*P*=0.001) in male *Eml*1 hom (and by 78.9% when analyzing n=2 females) . Remarkably, the areas of both the ventricular and subventricular zones (Cxne and SubVCx, respectively) were also smaller in males *Eml*$1^{-/-}$ mice (Cxne: -50.0%, *P*=0.006, SubVCx: -66.4%, *P*=0.0002, **Fig. 3A**). A similar tendency was observed in females. Unexpectedly, the lateral ventricles were smaller in size in male *Eml*$1^{-/-}$ mice (by 88.6%, *P*=0.0016, **Fig. 3A**). This trend was potentially mimicked in female *Eml*$1^{-/-}$ mice (n=2, smaller by 84.3%). This suggests that the hydrocephalus phenotype seen at 7 weeks of age is likely to originate from postnatal stages onwards, further supporting the hypothesis that independent mechanisms may be responsible for the different phenotypes observed (i.e. cortical anomalies versus hydrocephalus). The height of the cingulate cortex was reduced by 60.6% (P=0.0009) in male and by 39.5% (P=0.05) in female *Eml*1 hom mice (**Fig. 3A**). In contrast, some parameters were gender specific. For example, the apparent length of the pyramidal layer

For Peer Review Only

of the hippocampus was enlarged by 28.1% (*P*=0.0033) in male *Eml*$1^{-/-}$ mice, indicating that the hippocampal anomalies seen at 7 weeks of age might start in embryonic stages (**Fig. 3A**). The size of the anterior commissure appeared smaller in the two female *Eml*$1^{-/-}$ mice analyzed (-13.7%).

Characterization of the cortical heterotopia at E18.5

The band heterotopia (HeCo) was clearly visible and appeared to be interposed between the ICx and SubVCx zones of the developing cortex (**Fig. 3B**). The position and the general presentation of this subcortical heterotopia was consistent between the mice, however, its size varied more in female than in male *Eml*$1^{-/-}$ mice. To characterize the E18.5 heterotopia phenotype, we used the quantification of the same seven parameters as in adult and P13 mice which we adapted for embryonic stages (**Supp. Fig. 3C**), and analyzed cortices in *Eml*1 hom mice. The area and the height of the homotopic cortex was smaller in male *Eml*$1^{-/-}$ mice (for area: -27.5%, *P*=0.034; for height: -37.8%, *P*=0.0002), when compared to the normal total cortex (**Fig. 3C**). Similar trends were observed for females (n=2, for area -37.0%; for height, -37.1%). The combined area of HeCo and HoCo was either similar (male mice) or potentially smaller in female *Eml*$1^{-/-}$ mice when compared to matched WT brains (n=2, -20.6%). However, the thickness (height) of the combined HeCo and HoCo was moderately larger in male *Eml*$1^{-/-}$ mice (+16.2%, *P*=0.008, **Fig. 3C**), with a similar trend in females (n=2, +13.0%).

Taken together, these results suggest severe morphological anomalies in both male and female *Eml*1 hom mice. The origins of these anomalies are observed during embryonic development. The main anomalies were pertaining

For Peer Review Only

to the neocortex with the presence of a massive subcortical band heterotopia. Milder to moderate defects were also identified in other brain regions.

Absence of cortical heterotopia in *Eml*1 het mice but brain size defects

Next, we studied neuroanatomical features in both male and female *Eml1* het mice and confirmed the recessive transmission of the heterotopic cortex (Croquelois et al. 2009), since we did not see a single occurrence of heterotopia in the het state. However, we observed some brain size defects in male *Eml*1 het mice at both P13 and E18.5 stages (for male: **Fig. 2E, Fig. 3D;** for female: **Supp. Fig. 4A, 4B**). These anomalies may be more apparent in male mice due to the possible higher variation of phenotypic traits in females. The average effect size for significant brain parameters in male *Eml*1 het mice (n=3) was approximately half the size of the *Eml*1 hom mice. For example, the deep CxP area was reduced by 39.1% (*P*=0.02) in male *Eml*$1^{+/-}$ E18.5 mice (compared to a reduction of 79.4% in male *Eml*1 hom mice), together with a smaller SubVCx of -36.3% (*P*=0.0004), as compared to -66.4% (*P*=0.0002) in male *Eml*1 hom mice. This may suggest a gene dosage effect of *Eml*1 on certain aspects of developmental brain anatomy. Taken together, these results suggest a role for *Eml*1 in the regulation of brain size in a dosage dependent manner.

Ectopic RG progenitors in *Eml*1 KO mice at early stages of corticogenesis

Although heterotopia often arises because of aberrant neuronal migration, abnormalities in progenitor cells have also been associated with this cortical malformation (Bizzotto and Francis, 2015). In the spontaneous *Eml*1 mouse mutant, cycling progenitors were found outside the germinal layers, in basal

For Peer Review Only

regions of the cortical wall (Kielar et al. 2014, Bizzotto et al. 2017). These progenitors were often Pax6+, a marker of RGs, which are physiologically located in the neuroepithelial ventricular zone (Cxne). RGs are the main progenitor cells in the developing cortex, responsible for the production of other progenitor types and therefore the final neuronal output. Their apical processes extending to the ventricular surface (VS) are characterized by the presence of an adherens junctions-actin belt, which allows cell-cell interactions. Throughout the cell cycle, RG nuclei oscillate between the basal and apical-most region of the VZ, a process known as interkinetic nuclear migration. Basally they undergo S-phase, and mitosis takes place apically (Taverna et al. 2014, Uzquiano et al. 2018).

We assessed the location of cycling and Pax6+ progenitors at early stages of corticogenesis (E13.5). First, we analyzed the distribution of Ki67+ (a marker of proliferative cells), BrdU+ (incorporated during S-phase) cells in E13.5 cortices subjected to a 30 min. BrdU pulse. In order to assess cell distribution, ROIs were divided in six equally-sized bins across the cortical wall (**Fig. 4A**, top row, right panel). No major differences were observed between WT and het conditions, where Ki67+BrdU+ cells were mainly localized in basal regions of the Cxneas expected (bins 3 and 4, **Fig. 4A and 4C**). Hom mice (n=5) showed a significant increase in the percentage of Ki67+BrdU+ cells present in the SubVCx/ICx/CxP (bins 5 and 6) as well as in the apical-most Cxne (bin 1). Accordingly, there was a significant decrease in the percentage of cells expressing these markers in the most basal regions of the Cxne (**Fig. 4A and 4C**). This data shows the presence of aberrantly positioned cycling neuronal progenitors in *Eml*1 KO cortices.

For Peer Review Only

In order to assess the identity of aberrantly localized progenitors, we performed the same type of analyses with the RG marker Pax6. Whilst the vast majority of Pax6+ cells was localized in the Cxne in WT and het mice, a significant proportion of Pax6+ cells was shifted towards more basal positions (SubVCx/ICx/CxP, bins 5 and 6) in hom developing cortices (**Fig. 4B, 4D**). Therefore, our immunohistochemistry analyses at early stages of cortical development show the presence of ectopic Pax6+ and cycling progenitors.

Mouse mutants showing ectopically located Pax6+ progenitors can show disruption of the adherens junctions-actin belt delineating the VS (Cappello et al. 2006; Cappello et al. 2012; Gan et al. 2014; Gil-Sanz et al. 2014; Junghans et al. 2005; Kadowaki et al. 2007; Schmid et al. 2014). We performed immunostainings for N-Cadherin and F-actin, both markers for this belt. We confirm that no major changes were observed in *Eml*1 KO mice when compared to WT mice (**Supp. Fig. 4C**). Similar results were obtained previously for the spontaneous *Eml*1 mouse mutant (Kielar et al. 2014) suggesting that other primary mechanisms are likely to be responsible for the presence of ectopic Pax6+ progenitors in *Eml*1 mouse mutants.

For Peer Review Only

Discussion

A previous study described neuroanatomical defects in a spontaneous mouse mutant of *Eml*1 (Croquelois et al. 2009), a gene encoding a microtubule-associated protein, as a result of a retrotransposon insertion in the intron lying between exons 22 and 23 (Kielar et al. 2014). In this study, we analyzed the brain morphology of a new KO mouse model of *Eml*1, analyzing heterozygotes as well as homozygotes, and males as well as females. Overall, the anomalies we identified appeared more severe than the ones previously reported by spontaneous mutation on the NOR-CD1 genetic background (Croquelois et al. 2009). For example, the thickness of the homotopic cortex was reduced in the KO model in young adult and P13 animals (**Fig. 1D** and **Fig. 2C**), whereas it did not reach significance in the previously published spontaneous model (Croquelois et al. 2009). The combined thickness of the homotopic and heterotopic cortices was either unchanged, or only moderately larger in our study (**Fig. 1D**, **Fig. 2C and Fig. 3C**), but much larger in the previous report (Croquelois et al. 2009). Another example includes the subcortical band heterotopia that we detected at E18.5, whereas in the published spontaneous model, at a similar embryonic age, an increase of the intermediate zone of the cortex was described but not visibly the heterotopia (Croquelois et al. 2009). It should be noted however, that Croquelois et al mentioned in their study that a proportion of animals were observed with severer phenotypes. In our study we mainly analyzed single hemispheres but in cases where both hemispheres were analyzed (e.g. P13), the heterotopia was observed bilaterally.

Our results at early stages of corticogenesis (**Fig. 4**) show similar results to those observed in the spontaneous *Eml*1 mouse mutant (Kielar et al, 2014). In *Eml*1 KO cortices we also observe the presence of ectopic cycling neuronal progenitors, further supporting that this progenitor displacement may be the original defect leading to the heterotopia phenotype in *Eml*1-mutant conditions. The heterotopia develops from this point on, with accumulating neurons in the ICx, at the expense of those in the CxP.

The neuroanatomical anomalies we identified may point to a possible sexual dimorphism. Whilst male and female mice appeared to share similar

For Peer Review Only

phenotypes, variability in the female group, which also included apparently individuals without heterotopia, suggests a more complex pattern of inheritance. Indeed, in two *Eml*1 hom young adult females, the subcortical band heterotopia was completely absent, and in E18.5 females (n=2 analyzed), the size of the subcortical band heterotopia seemed to be more heterogeneous than in males. Although we do not rule out that heterotopia may be smaller or unilateral, overall, the phenotypes seem different in males. The reasons for potential male-female differences remain unclear but may reflect the genetic background used, possibly involving modifier genes, and/or hormones, leading to a less severe brain phenotype in females. Interestingly as well, at E18.5 and P13, subtle brain size defects may exist only in male heterozygotes. However, few heterozygote defects were detected at 7 weeks of age, which may suggest that these developmental anomalies represent delayed processes that catch up over time. However, caution is also still required in drawing conclusions, since sampling may be insufficient to capture the full picture of inter-individual and inter-litter variations.

Our morphological screen of the KO on this genetic background allowed us to associate Eml1 function with spatially distinct brain defects, suggesting a role for the *Eml*1 gene in the overall architecture of the brain. This is consistent with the wider expression pattern of *Eml*1 in different types of neuronal progenitors and post mitotic neurons during development (Kielar et al. 2014). Although no defects were reported in the spontaneous model of *Eml*1 in structures such as the hippocampus, the striatum, the thalamus and the cerebellum (Kielar et al. 2014), we found perturbations in the KO including corpus callosum agenesis and hydrocephalus, as well as in the organization

For Peer Review Only

and/or size of hippocampal regions, at embryonic, postnatal and adult stages. Interestingly, the *BXD29* mouse model for subcortical heterotopia shows ectopic clusters of neurons in CA1 and the dentate gyrus (Ramos et al. 2016). Additionally, other mouse mutants for genes mutated in severe forms of human heterotopia (*Dcx, Lis1, Tuba1a*) (Barkovich et al. 2012, des Portes et al. 1998, Gleeson et al. 1998) also show a heterotopia-like phenotype in the hippocampus in the form of a ‘double-layer’ in the CA3 region (Corbo et al. 2002; Hirotsune et al. 1998; Kappeler et al. 2007; Keays et al. 2007). It is thus of interest that CA3 cell dispersion was detected in the *Eml*1 KO model, and future work involving serial sections across the brain will attempt to confirm this phenotype.

Related to the hydrocephalus phenotype here described, a mild ventricular enlargement was previously reported in the *HeCo* mouse (Croquelois et al. 2009). Additionally, 2 out of 3 *EML*1-mutation families present hydrocephalus (Kielar et al. 2014, Shaheen et al. 2017). Further studies of *Eml*1 hom mice at postnatal stages may help unravel the underlying pathological mechanisms resulting in the hydrocephalus. Additionally, further postnatal studies are required to investigate causes of death of *Eml*1 hom mice and their relationships with brain morphology.

Rodent models of heterotopia, originally thought to be quite rare, are now becoming available to provide further information on how heterotopia form and disrupt neuronal function (reviewed in Bizzotto and Francis, 2015, Stouffer et al. 2016). This new constitutive KO, finely characterized here, is a valuable tool to contribute further to this domain.

For Peer Review Only

Acknowledgements

We are grateful to the French Fondation Maladies Rares for agreeing to fund this project. We would like to thank the Genetic Engineering and Model Validation Department at the ICS for generating the mouse model; the animal care-takers of the PHENOMIN-ICS animal facility for their technical assistance with mouse care. We would like to thank the Imaging Platform at the Institut du Fer à Moulin, Paris, as well as Dr. Marika-Nosten Bertrand for advice with statistical analyses. Finally we would like to thank Patrick Reilly, Yann Herault and Tania Sorg from the ICS.

Conflict of Interest statement. None declared.

Funding

AU and FF are associated with the BioPsy Labex project and the Ecole des Neurosciences de Paris Ile-de-France (ENP) network. Our labs are supported by Inserm, Centre national de la recherche scientifique (CNRS), UPMC, French Agence National de la Recherche (ANR-13-BSV4-0008-01; ANR-16-CE16-0011-03), Fondation Bettencourt Schueller, the European Union (EU-HEALTH-2013, DESIRE, No 60253) to FF, the JTC 2015 Neurodevelopmental Disorders, the ANR (for NEURON8-Full- 815-006 STEM-MCD), the Fondation Maladies Rares/Phenomin (project IR4995), and the European Cooperation on Science and Technology (COST Action CA16118) to FF. BY is supported by a French State fund grant (ANR-10-LABX-0030-INRT), managed by the Agence Nationale de la Recherche under the frame program Investissements d'Avenir

For Peer Review Only

ANR-10-IDEX-0002-02. AU received an ENP PhD grant, a Company of Biologists travel grant, and is currently funded by the Fondation de France. This study received support from French state funds through the ANR under the frame programme Investissements d'Avenir labelled ANR-10-INBS-07 PHENOMIN.

Bibliography

Bahi-Buisson, N., Souville, I., Fourniol, F. J., Toussaint, A., Moores, C. A., Houdusse, A., Lemaitre, J. Y., Poirier, K., Khalaf-Nazzal, R., Hully, M., Leger, P. L. (2013). New insights into genotype-phenotype correlations for the doublecortin-related lissencephaly spectrum. *Brain* 136 (Pt 1): 223-244.

Barkovich, A.J., Guerrini, R., Kuzniecky, R.I., Jackson, G.D. and Dobyns, W.B. (2012) A developmental and genetic classification for malformations of cortical development: update 2012. *Brain*. 135, 1348–1369.

Beattie, R., M. P. Postiglione, L. E. Burnett, S. Laukoter, C. Streicher, F. M. Pauler, G. Xiao, O. Klezovitch, V. Vasioukhin, T. H. Ghashghaei and S. Hippenmeyer (2017). Mosaic Analysis with Double Markers Reveals Distinct Sequential Functions of Lgl1 in Neural Stem Cells. *Neuron* 94(3): 517-533 e513.

Birling, M.C., Dierich, A., Jacquot, S., Hérault, Y., Pavlovic, G. (2012) Highly-efficient, fluorescent, locus directed cre and FlpO deleter mice on a pure C57BL/6N genetic background. *Genesis*, 50(6):482-9. doi: 10.1002/dvg.20826.

Bizzotto S. and Francis F. (2015) Morphological and functional aspects of progenitors perturbed in cortical malformations. *Front Cell Neurosci*. 9, 30.

For Peer Review Only

Bizzotto, S., Uzquiano, A., Dingli, F., Ershov, D., Houllier, A., Arras, G., Richards, M., Loew, D., Minc, N., Croquelois, A., Houdusse, A., Francis, F. (2017) Eml1 loss impairs apical progenitor spindle length and soma shape in the developing cortex. *Sci. Rep*. 7:17308.

Cappello S., Attardo A., Wu X. et al. (2006) The Rho-GTPase cdc42 regulates neural progenitor fate at the apical surface. *Nat. Neurosci*. 9, 1099–1107.

Cappello S., Bohringer C. R., Bergami M. et al. (2012) A radial glia-specific role of RhoA in double cortex formation. *Neuron*, 73, 911–924.

Collins, S*.*, Wagner, C., Gagliardi, L., Kretz, P. F., Fischer M. C., Kessler, P., Kannan, M., Yalcin, B*.* (2018) Benefits of using parasagittal over coronal sectionning for neuroanatomical quantification of the adult brain structure in the mouse. *Curr Protoc Mouse Biol*. 8(3):e48. doi: 10.1002/cpmo.48.

Corbo, J.C., Deuel, T.A., Long, J.M., LaPorte, P., Tsai, E., Wynshaw-Boris, A. and Walsh, C.A. (2002) Doublecortin is required in mice for lamination of the hippocampus but not the neocortex. *J. Neurosci*. 22, 7548–7557.

Croquelois, A., Giuliani, F., Savary, C., Kielar, M., Amiot, C., Schenk, F., Welker, E. (2009) Characterization of the HeCo mutant mouse: a new model of subcortical band heterotopia associated with seizures and behavioral deficits. *Cereb Cortex* 19(3):563-575.

desPortes,V., Francis, F., Pinard,J. M. ,Desguerre, I. ,Moutard, M.L., Snoeck, I., Meiners, L.C., Capron, F., Cusmai, R., Ricci, S., et al. (1998) doublecortin is the major gene causing X-linked subcortical laminar heterotopia (SCLH). *Hum. Mol. Genet*. 7, 1063–1070.

For Peer Review Only

Farrell, M. A., DeRosa, M. J., Curran, J. G., Secor, D. L., Cornford, M. E., Comair, Y. G., et al. (1992). Neuropathologic findings in cortical resections (including hemispherectomies) performed for the treatment of intractable childhood epilepsy. *Acta Neuropathol* 83: 246-259.

Gan, Q., Lee, A., Suzuki, R., Yamagami, T., Stokes, A., Nguyen, B. C., Pleasure, D., Wang, J., Chen, H. W. and Zhou, C. J. (2014) Pax6 mediates ss-catenin signaling for self-renewal and neurogenesis by neocortical radial glial stem cells. *Stem Cells,* 32, 45–58.

Gil-Sanz, C., Landeira, B., Ramos, C., Costa, M. R. and Muller, U. (2014) Proliferative defects and formation of a double cortex in mice lacking Mltt4 and Cdh2 in the dorsal telencephalon. *J. Neurosci*. 34, 10475–10487.

Gleeson, J.G., Allen, K.M., Fox, J.W., Lamperti, E.D., Berkovic, S., Scheffer, I., Cooper, E.C., Dobyns, W.B., Minnerath, S.R., Ross, M.E., et al. (1998) Doublecortin, a brain-specific gene mutated in human X-linked lissencephaly and double cortex syndrome, encodes a putative signaling protein. *Cell*, 92, 63–72.

Götz, M., Huttner, W. (2005). The cell biology of neurogenesis. N*at Rev Cell Biol*. 6 (10), 777-7888.

Guerrini, R. (2005). Genetic malformations of the cerebral cortex and epilepsy. *Epilepsia* 46 Suppl 1: 32–37.

Jossin, Y., M. Lee, O. Klezovitch, E. Kon, A. Cossard, W. H. Lien, T. E. Fernandez, J. A. Cooper and V. Vasioukhin (2017). Llgl1 Connects Cell Polarity

For Peer Review Only

with Cell-Cell Adhesion in Embryonic Neural Stem Cells. *Dev Cell* 41(5): 481-495 e485.

Junghans, D., Hack, I., Frotscher, M., Taylor, V. and Kemler, R. (2005) Beta-catenin-mediated cell-adhesion is vital for embryonic forebrain development. *Dev. Dyn*. 233, 528–539.

Kadowaki, M., Nakamura, S., Machon, O., Krauss, S., Radice, G. L. and Takeichi, M. (2007) N-cadherin mediates cortical organization in the mouse brain. *Dev. Biol*. 304, 22–33.

Kappeler, C., Dhenain, M., Phan Dinh Tuy, F., Saillour, Y., Marty, S., Fallet-Bianco, C., Souville, I., Souil, E., Pinard, J.M., Meyer, G., et al. (2007) Magnetic resonance imaging and his- tological studies of corpus callosal and hippocampal abnormalities linked to doublecortin deficiency. *J. Comp. Neurol.* 500, 239–254.

Keays, D.A., Tian, G., Poirier, K., Huang, G.J., Siebold, C., Cleak, J., Oliver, P.L., Fray, M., Harvey, R.J., Molnar, Z., et al. (2007) Mutations in alpha-tubulin cause abnormal neuronal migration in mice and lissencephaly in humans. *Cell*, 128, 45–57.

Kielar M*, et al.* (2014) Mutations in Eml1 lead to ectopic progenitors and neuronal heterotopia in mouse and human. *Nat Neurosci* 17(7):923-933.

Matsuzaki, F. and Shitamukai, A. (2015) Cell division modes and cleavage planes of neural progenitors during mammalian cortical development. *Cold Spring Harb. Perspect. Biol*. 7, a015719.

Meencke, H. J., and Veith, G. (1992). Migration disturbances in epilepsy. *Epilepsy Res*. Suppl. 9: 31-40.

For Peer Review Only

Mikhaleva, A., Kannan, M., Wagner, C., Yalcin, B. (2016) Histomorphological Phenotyping of the Adult Mouse Brain. *Curr Protoc Mouse Biol.* 6(3):307-332.

Molyneaux, B., Arlotta, P., Menezes, J. R., Macklis, J. D. (2007) Neuronal subtype speficiation in the cerebral cortex.

Liu, W. A., S. Chen, Z. Li, C. H. Lee, G. Mirzaa, W. B. Dobyns, M. E. Ross, J. Zhang and S. H. Shi (2018). PARD3 dysfunction in conjunction with dynamic HIPPO signaling drives cortical enlargement with massive heterotopia. *Genes Dev* 32(11-12): 763-780.

Palmer, T.D., Willhoite, A. R., Gage, F. G. (2000) Vascular niche for adult hippocampal neurogenesis. *J. Comp. Neurol*. 425, 479-494

Ramos, R. L., Toia, A. R., Pasternack, D. M., Dotzler, J. A. C., Esposito, A. W., Le, M. M., Parker, A. K., Goodman, J. H., Sarkisian, M. R. (2016) Neuroanatomical characterization of the cellular and axonal architecture of subcortical band heterotopia in the BXD29-Tlr4$^{lps\text{-}2J}$/J mouse cortex. *Neuroscience*, 337, 48-65.

Richards, M. W., O'Regan, L., Roth, D., Montgomery, J. M., Straube, A. Fry, M., Bayliss, R. (2015) Microtubule association of EML proteins and the EML4-ALK variant 3 oncoprotein require an N-terminal trimerization domain. *Biochem. J.* 437 (3), 529-536.

Romero, D. M., Bahi-Buisson, N. and Francis, F. (2018) Genetics and mechanisms leading to human cortical malformations. *Semin. Cell Dev. Biol.* 76, 33–75.

For Peer Review Only

Shaheen, R., Sebai, M. A., Patel, N., Ewida, N., Kurdi, W., Altweijri, I., Sogaty, S., Almardawi, E., Seidahmed, M. Z., Alnemri, A., et al. (2017) The genetic landscape of familial congenital hydrocephalus. *Ann. Neurol*. 81, 890-897.

Schmid M. T., Weinandy F., Wilsch-Brauninger M., Huttner W. B., Cappello S. and Gotz M. (2014) The role of alpha-E-catenin in cerebral cortex development: radial glia specific effect on neuronal migration. *Front Cell Neurosci*. 8, 215.

Stouffer, M. A., Golden, J. A. and Francis, F. (2016) Neuronal migration disorders: focus on the cytoskeleton and epilepsy. *Neurobiol. Dis.* 92, 18–45.

Taverna, E., Gotz, M. and Huttner, W.B. (2014). The cell biology of neurogenesis: toward an understanding of the development and evolution of the neocortex. *Annu Rev Cell Dev Biol*, 30, 465-502.

Uzquiano, A., Gladwyn-Ng, I., Nguyen, L., Reiner, O., Gotz, M., Matsuzaki, F., Francis, F. (2018) Cortical progenitor biology, cell cycling versus neurogenesis. *J. Neurochem*. doi: 10.1111/jnc.14338

For Peer Review Only

Figure legends

Figure 1 Juvenile *Eml*1 KO mouse shows a giant subcortical band heterotopia, abnormal hippocampus, hydrocephalus and corpus callosum agenesis (**A**) Schematic representation of affected brain regions in *Eml*$1^{-/-}$ male (left) and female (right) mice at 7 weeks of age plotted in sagittal planes according to p-values. The top image represents a section at Lateral +0.60 mm. The color map indicates p-values below the threshold of 0.05 whereas grey indicates parameters for which statistics could not be computed (sample size below 3) and white indicates non-significance. Histograms show the percentage decreased (minus scale) or increased (plus scale) of measured brain regions as compared to the controls (0%). They are combined with box plots displaying the median with interquartile range. Each point represents an animal. Certain data remain preliminary given that n<3 male mice for one or both genotypes were compared for the following areas: medial cerebellar nucleus, caudate-putamen, optic chiasm, ventromedial hypothalamus nucleus, substantia nigra, fornix, pontine nuclei, transverse fibers of the pons, cingulate cortex area and cingulate cortex height, and n<3 females were compared for the following areas: total brain, brain height, temporal cortex, pons height, cerebellum, internal granule layer, medial cerebellar nucleus, corpus callosum height, caudate-putamen, anterior commissure, stria medullaris, substantia nigra, optic chiasm, transverse fibers of the pons, cingulate cortex and cingulate cortex height. (**B**) Nissl-stained sagittal brain sections from *Eml*1$^{-/-}$ mouse, showing a giant band of subcortical heterotopic neurons, dispersed neurons in the CA3 layer of the hippocampus and enlarged dorsal subiculum (indicated by black arrows). (**C**) Schematic representation of brain regions in *Eml*1$^{+/-}$ male mice at 7 weeks of age plotted in sagittal planes according to p-values. Data concerning the following areas remain preliminary given the lower n numbers (i.e. n<3): caudate-putamen, optic chiasm, ventromedial hypothalamus nucleus, pontine nuclei, substantia nigra, transverse fibers of the pons, inferior colliculus, superior colliculus, and brain height. (**D**) Characterization of the heterotopic cortex (HeCo) as well as the homotopic cortex (HoCo) in *Eml*1$^{-/-}$ male and female mice (n=2 for *Eml*1$^{-/-}$ female mice). The description of the parameters used is provided in **Supp. Fig. 2C**. Plots are represented as mean

For Peer Review Only

±SEM. * $P<0.05$, ** $P<0.005$, *** $P<0.005$ (Student's *t* test, two-tailed) for the comparison between HoCo and Cx (normal cortex in WT). (**E**) Details of brain regions assessed in order of appearance in Panel A together with corresponding numbers.

Figure 2 *Eml*1 KO mouse shows similar defects at postnatal day 13 (**A**) Schematic representation of affected brain regions in *Eml*1$^{-/-}$ male (left) and female (right) mice at P13 plotted in sagittal planes according to p-values. The top image represents a section at Lateral +0.60 mm. The color map indicates p-value below the threshold of 0.05 and grey indicates parameters where the n was too low to perform statistics. Histograms show the percentage decreased (minus scale) or increased (plus scale) of measured brain regions as compared to the controls (0%). They are combined with box plots displaying the median with interquartile range. Each point represents an animal. Certain data remain preliminary given that $n<3$ male mice for one or both genotypes were compared for the following areas: total brain, cerebellum, internal granular layer, medial cerebellar nucleus, lateral ventricle, caudate-putamen, stria medullaris, fornix, optic chiasm, ventromedial hypothalamus nucleus, pontine nuclei, substantia nigra, transverse fibers of the pons, cingulate cortex, dorsal subiculum, inferior colliculus, superior colliculus, brain height and pons height, and $n<3$ females were compared for the following areas: temporal cortex, cerebellum, internal granular layer, medial cerebellar nucleus, lateral ventricle, caudate-putamen, anterior commissure, stria medullaris, fornix, optic chiasm, ventromedial hypothalamus nucleus, pontine nuclei, substantia nigra, transverse fibers of the pons, inferior colliculus, superior colliculus, brain height, primary motor cortex

For Peer Review Only

height and cingulate cortex height. (**B**) Nissl-stained sagittal brain sections from *Eml1*$^{-/-}$ mouse, showing a giant band of subcortical heterotopic neurons, dispersed neurons in the CA3 layer of the hippocampus and enlarged dorsal subiculum. (**C**) Characterization of the heterotopic cortex (HeCo) as well as the homotopic cortex (HoCo) in *Eml*1$^{-/-}$ male and female mice. Plots are represented as mean ±SEM. * P<0.05, ** P<0.005, *** P<0.005 (Student's *t* test, two-tailed) for the comparison between HoCo and Cx (normal cortex in WT), and § P<0.05, §§ P<0.005 for the comparison between HoCo+HeCo and Cx. (**D**) Immunostainings for Tbr1 at P13 in male and female WT, het and hom mice. Tbr1 (green) and DAPI (blue). White dashed lines delineate the heterotopia (*). Scale bar: 100 μm (**E**) Schematic representation of brain regions in *Eml*1$^{+/-}$ male mice at P13 plotted in sagittal planes according to p-values. Histograms and box plots illustrate the results as described for A. Data concerning the following areas remain preliminary given n<3 numbers for one or both genotypes: total brain, cerebellum, internal granular layer, medial cerebellar nucleus, lateral ventricle, caudate-putamen, dentate gyrus, stria medullaris, fornix, optic chiasm, ventromedial hypothalamus nucleus, pontine nuclei, substantia nigra, transverse fibers of the pons, cingulate cortex, dorsal subiculum, inferior colliculus, superior colliculus, as well as the following parameters: total brain height, primary motor cortex length, radiatum layer of the hippocampus length and pons height.

Figure 3 Late embryonic *Eml1* KO mouse exhibits subcortical band heterotopia but not enlarged ventricle size (**A**) Histograms comparing E18.5 male and female *Eml*1$^{-/-}$ to matched WT and showing variation (decreased-

For Peer Review Only

minus scale or increased-positive scale) in areas and lengths expressed as percentage of WT together with a color map indicating the significance level. They are combined with box plots displaying the median with interquartile range. Each point represents an animal. Certain data remain preliminary given that n<3 male mice for one or both genotypes were compared for the following areas: caudate-putamen, fornix, stria medullaris, optic chiasm, pontine nuclei and pons heigtht, and n<3 females were compared for the following areas: total midbrain, subventricular cortex, intermediate cortex, lower cortical plate, caudate-putamen, anterior commissure, fornix, stria medullaris, optic chiasm, inferior colliculus, superior colliculus, mesencephalic reticular formation, pontine nuclei, cerebellum, lateral ventricles, total brain height, subventricular cortex height, intermediate cortex height, lower cortical plate height and pons height (left panel). A schematic representation of a section at Lateral +0.60mm with the colored regions indicating the presence of at least one significant parameter within the brain region (right panel). White coloring indicates a p-value higher than 0.05 and grey shows not enough data to calculate a p-value. (**B**) Representative Nissl-stained sagittal brain sections from E18.5 *Eml*$1^{-/-}$ mouse (bottom panels), showing a giant band of subcortical heterotopic neurons (black arrow), compared to a WT section (top panels). (**C**) Characterization of the size and the average thickness of the homotopic (HoCo) and the heterotopic (HeCo) cortices in E18.5 *Eml1*$^{-/-}$ male mice (top panels) and E18.5 *Eml*$1^{-/-}$ female mice (bottom panels). The description of the parameters used is provided in **Supp. Fig. 3B**. Plots are represented as mean ±SEM. * P<0.05, ** P<0.005, *** P<0.005 (Student's *t* test, two-tailed) for the comparison between HoCo and Cx (normal cortex in WT), and § P<0.05, for the comparison

For Peer Review Only

between HoCo+HeCo and Cx. (**D**) Histograms and box plots comparing E18.5 male *Eml*1$^{+/-}$ to matched WT as described for A. A schematic representation of a section at Lateral +0.60mm with the colored regions indicating the presence of at least one significant parameter within the brain region (right panel). White coloring indicates a p-value higher than 0.05 and grey shows not enough data to calculate a p-value. Data concerning the following areas remain preliminary given the low n numbers (i.e. $n<3$): total midbrain, caudate-putamen, fornix, fimbria, stria medullaris, optic chiasm, inferior colliculus, superior colliculus, mesencephalic reticular formation, pontine nucleus and lateral ventricles.

For Peer Review Only

Figure 4 *Eml*1 KO mice show ectopic progenitors at early stages of corticogenesis. (A) Representative images of WT (top row), het (middle row) and hom (bottom row) cortices at E13.5, immunostained for Ki67 (green) and BrdU (red) after a 30 min pulse of the latter. The diverse regions of the developing cortical wall are indicated in the first image of the top row (WT). An example of the binning procedure is shown in the last image of the top row (WT). (B) Representative images of WT (top row), het (middle row) and hom (bottom row) cortices at E13.5, immunostained for Pax6 (red) and Hoechst (blue). (C) Quantification of percentage of Ki67+BrdU+ cells present in each of the six bins. (D) Quantification of percentage of Pax6+ cells present in each of the six bins. Bins 1-4 span across the ventricular zone (Cxne or VZ). Bins 5-6 span across the subventricular zone (SVZ or SubVCx), intermediate zone (IZ or ICx) and cortical plate (CP or CxP). Scale bar: 10 µm. The median is represented and the error bars represent the minimum and maximum range.

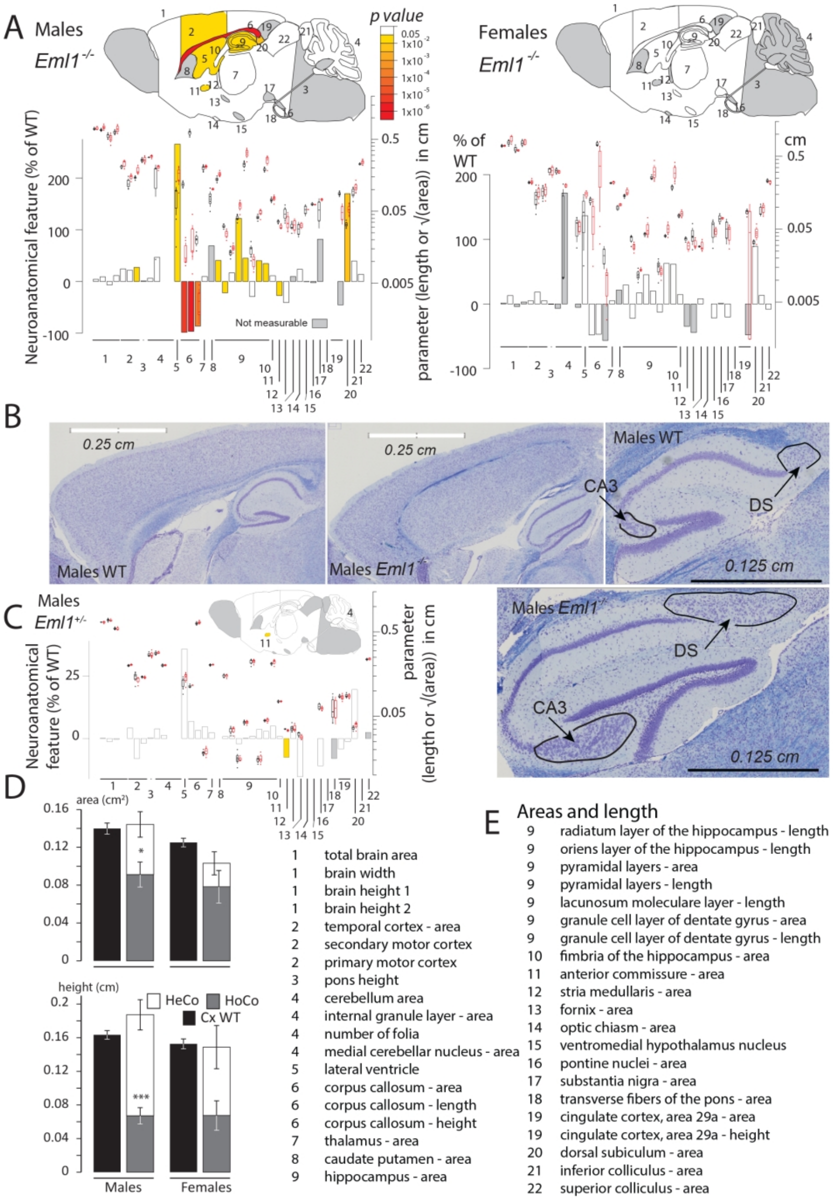

Areas and length

1	total brain area
1	brain width
1	brain height 1
1	brain height 2
2	temporal cortex - area
2	secondary motor cortex
2	primary motor cortex
3	pons height
4	cerebellum area
4	internal granule layer - area
4	number of folia
4	medial cerebellar nucleus - area
5	lateral ventricle
6	corpus callosum - area
6	corpus callosum - length
6	corpus callosum - height
7	thalamus - area
8	caudate putamen - area
9	hippocampus - area
9	radiatum layer of the hippocampus - length
9	oriens layer of the hippocampus - length
9	pyramidal layers - area
9	pyramidal layers - length
9	lacunosum moleculare layer - length
9	granule cell layer of dentate gyrus - area
9	granule cell layer of dentate gyrus - length
10	fimbria of the hippocampus - area
11	anterior commissure - area
12	stria medullaris - area
13	fornix - area
14	optic chiasm - area
15	ventromedial hypothalamus nucleus
16	pontine nuclei - area
17	substantia nigra - area
18	transverse fibers of the pons - area
19	cingulate cortex, area 29a - area
19	cingulate cortex, area 29a - height
20	dorsal subiculum - area
21	inferior colliculus - area
22	superior colliculus - area

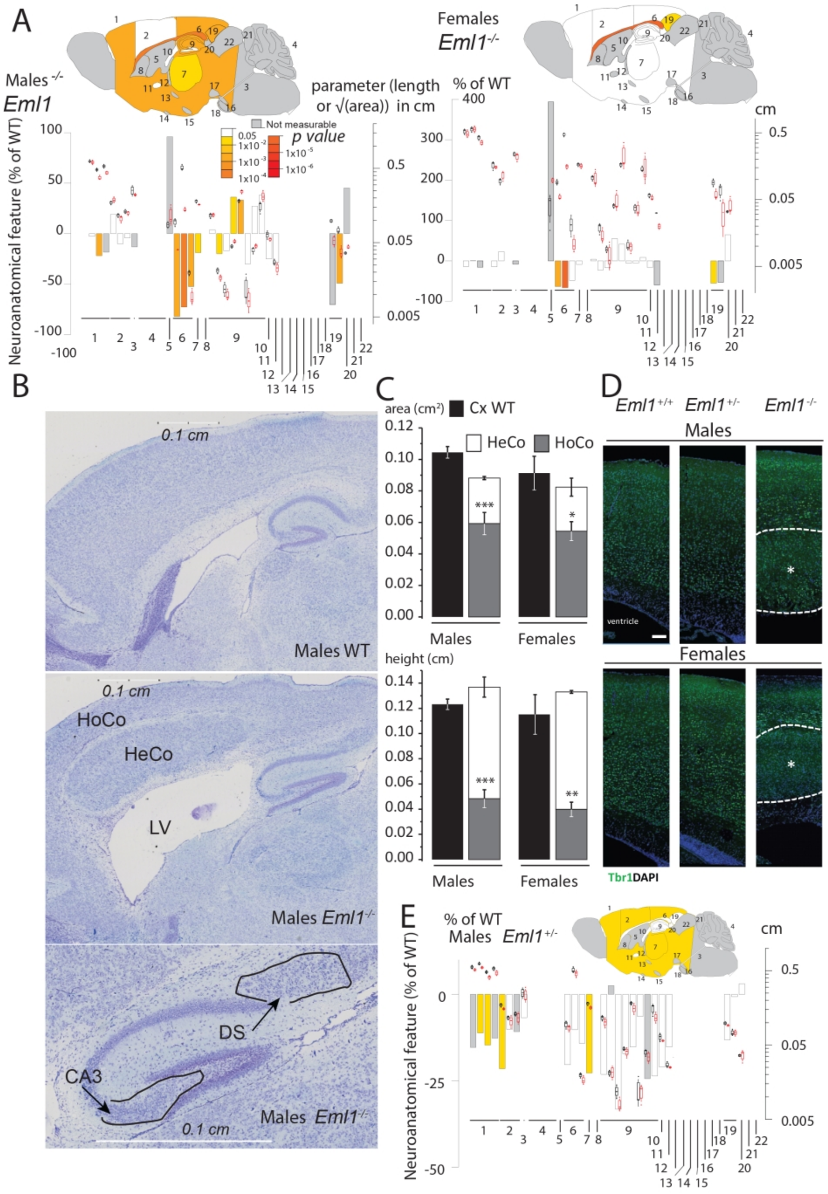
A
Males -/-
Eml1
Females
Eml1-/-
Neuroanatomical feature (% of WT)
parameter (length or √(area)) in cm
% of WT
cm
Not measurable
p value
0.05
1x10-2
1x10-3
1x10-4
1x10-5
1x10-6
B
0.1 cm
Males WT
HoCo
HeCo
LV
Males Eml1-/-
DS
CA3
C
area (cm²)
Cx WT
HeCo
HoCo
Males
Females
height (cm)
D
Eml1+/+
Eml1+/-
Eml1-/-
Males
Females
ventricle
Tbr1DAPI
E
% of WT
Males Eml1+/-
Neuroanatomical feature (% of WT)
cm

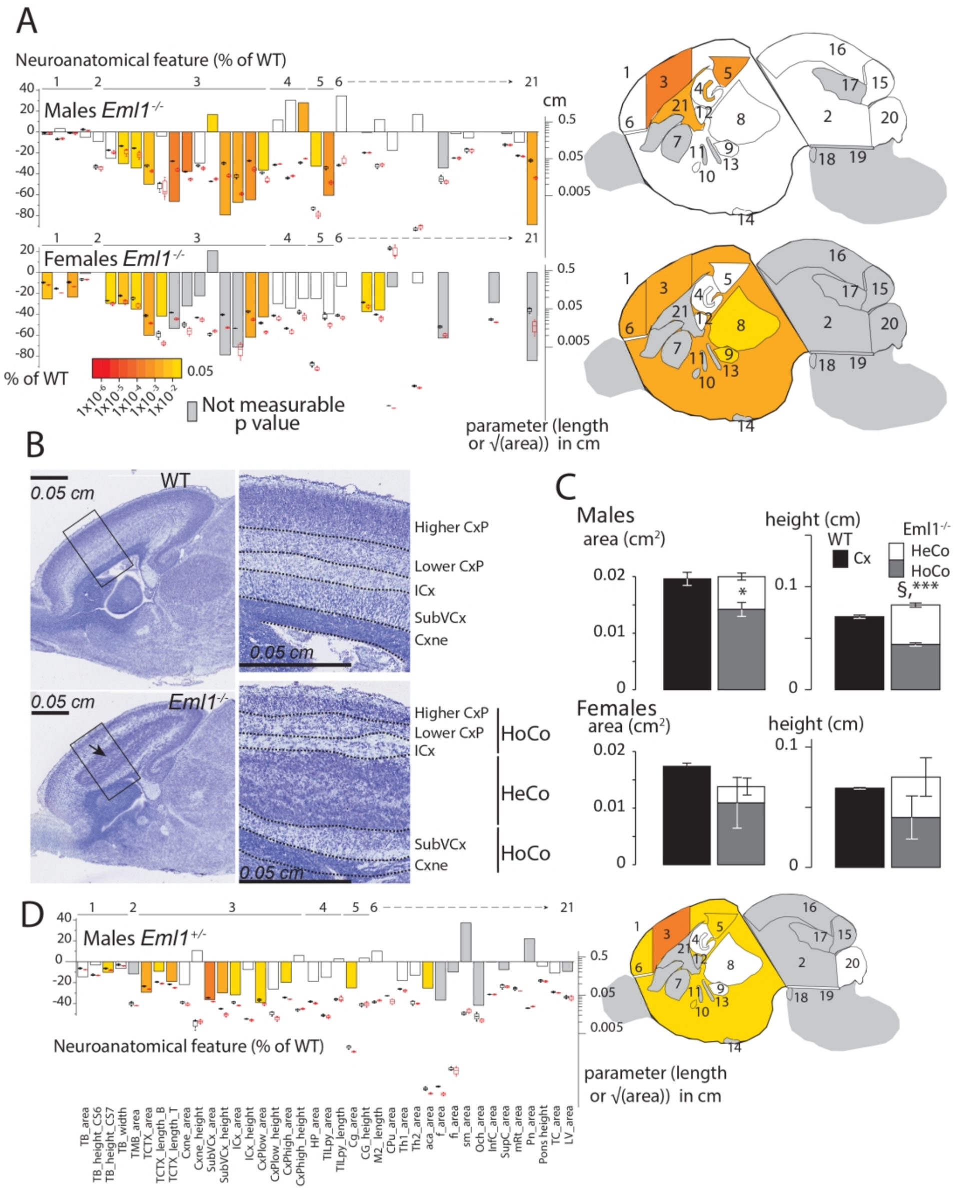
A
Neuroanatomical feature (% of WT)
Males Eml1-/-
Females Eml1-/-
1 2 3 4 5 6 21
40 20 0 -20 -40 -60 -80
% of WT
cm
0.5 0.05 0.005
1x10-6 1x10-5 1x10-4 1x10-3 1x10-2 0.05
p value
Not measurable
parameter (length or √(area)) in cm
1 2 3 4 5 6 7 8 9 10 11 12 13 14 15 16 17 18 19 20 21
B
WT
Eml1-/-
0.05 cm
Higher CxP
Lower CxP
ICx
SubVCx
Cxne
HoCo
HeCo
C
Males
Females
area (cm2)
height (cm)
0.02 0.01 0
0.1 0
WT
Cx
Eml1-/-
HeCo
HoCo
*
§,***
D
Males Eml1+/-
40 20 0 -20 -40
0.5 0.05 0.005
Neuroanatomical feature (% of WT)
parameter (length or √(area)) in cm
TB_area
TB_height_CS6
TB_height_CS7
TB_width
TMB_area
TCTX_area
TCTX_length_B
TCTX_length_T
Cxne_area
Cxne_height
SubVCx_area
SubVCx_height
ICx_area
ICx_height
CxPlow_area
CxPlow_height
CxPhigh_area
CxPhigh_height
HP_area
TILpy_area
TILpy_length
Cg_area
CG_height
M2_length
CPu_area
Th1_area
Th2_area
aca_area
f_area
fi_area
sm_area
Och_area
InfC_area
SupC_area
mRt_area
Pn_area
Pons height
TC_area
LV_area

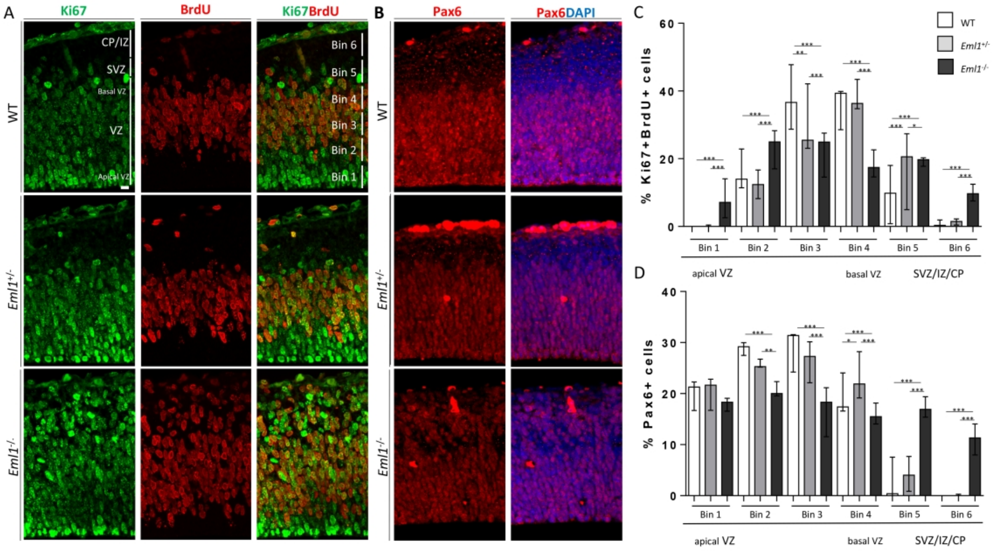
A
Ki67
BrdU
Ki67BrdU
WT
Eml1+/-
Eml1-/-
CP/IZ
SVZ
Basal VZ
VZ
Apical VZ
Bin 6
Bin 5
Bin 4
Bin 3
Bin 2
Bin 1
B
Pax6
Pax6DAPI
WT
Eml1+/-
Eml1-/-
C
WT
Eml1+/-
Eml1-/-
% Ki67+BrdU+ cells
0
20
40
60
Bin 1
Bin 2
Bin 3
Bin 4
Bin 5
Bin 6
apical VZ
basal VZ
SVZ/IZ/CP
D
% Pax6+ cells
0
10
20
30
40
Bin 1
Bin 2
Bin 3
Bin 4
Bin 5
Bin 6
apical VZ
basal VZ
SVZ/IZ/CP

The neuroanatomy of *Eml*1 knockout mice, a model of subcortical heterotopia

Stephan C. Collins[1-5]#, **Ana Uzquiano**[6-8]#, **Mohammed Selloum** [1, 2, 3, 4, 9], **Olivia Wendling** [1, 2, 3, 4, 9], **Marion Gaborit**[1-4], **Maria Ossipenko**[1-4], **Marie-Christine Birling** [1, 2, 3, 4, 9], **Binnaz Yalcin**[1-4]*, **Fiona Francis**[6-8]*

[1] Institut de Génétique et de Biologie Moléculaire et Cellulaire, Illkirch, France.
[2] Centre National de la Recherche Scientifique, UMR7104, Illkirch, France.
[3] Institut National de la Santé et de la Recherche Médicale, U964, Illkirch, France.
[4] Université de Strasbourg, Illkirch, France.
[5] Centre des Sciences du Goût et de l'Alimentation, Université de Bourgogne-Franche Comté, Dijon, France.
[6] INSERM UMR S-1270, Paris, France
[7] Sorbonne Université, UMR S-1270, F-75005 Paris, France
[8] Institut du Fer à Moulin, Paris, France
[9] CELPHEDIA, PHENOMIN, Institut Clinique de la Souris (ICS), 1 rue Laurent Fries, F-67404 Illkirch-Graffenstaden, France

# Contributed equally to this work

* To whom correspondence should be addressed

For Peer Review Only

Supplementary tables

Supplementary Table 1 Description of the 166 variables for adult brain sagittal analysis at Lateral 600 μm (right hemisphere). Column A gives the acronym of the brain parameter, column B its description, and column C the unit of the measurement.

Supplementary Table 2 List of 39 variables for brain sagittal analysis at E18.5 Lateral 600 μm (right hemisphere). Column A gives the type of the analysis. Column B is the name of the section of interest (named "critical" section) on which the analysis was done. Column C gives the corresponding brain region analyzed. Column D is the acronym of the assessed parameter (9 refers to the right hemisphere, we keep the left hemisphere for storage). Column E, F and G provide the full description of the parameter, the category of the measurement and its unit, respectively.

For Peer Review Only

Supplementary Figures

Supplementary Figure 1

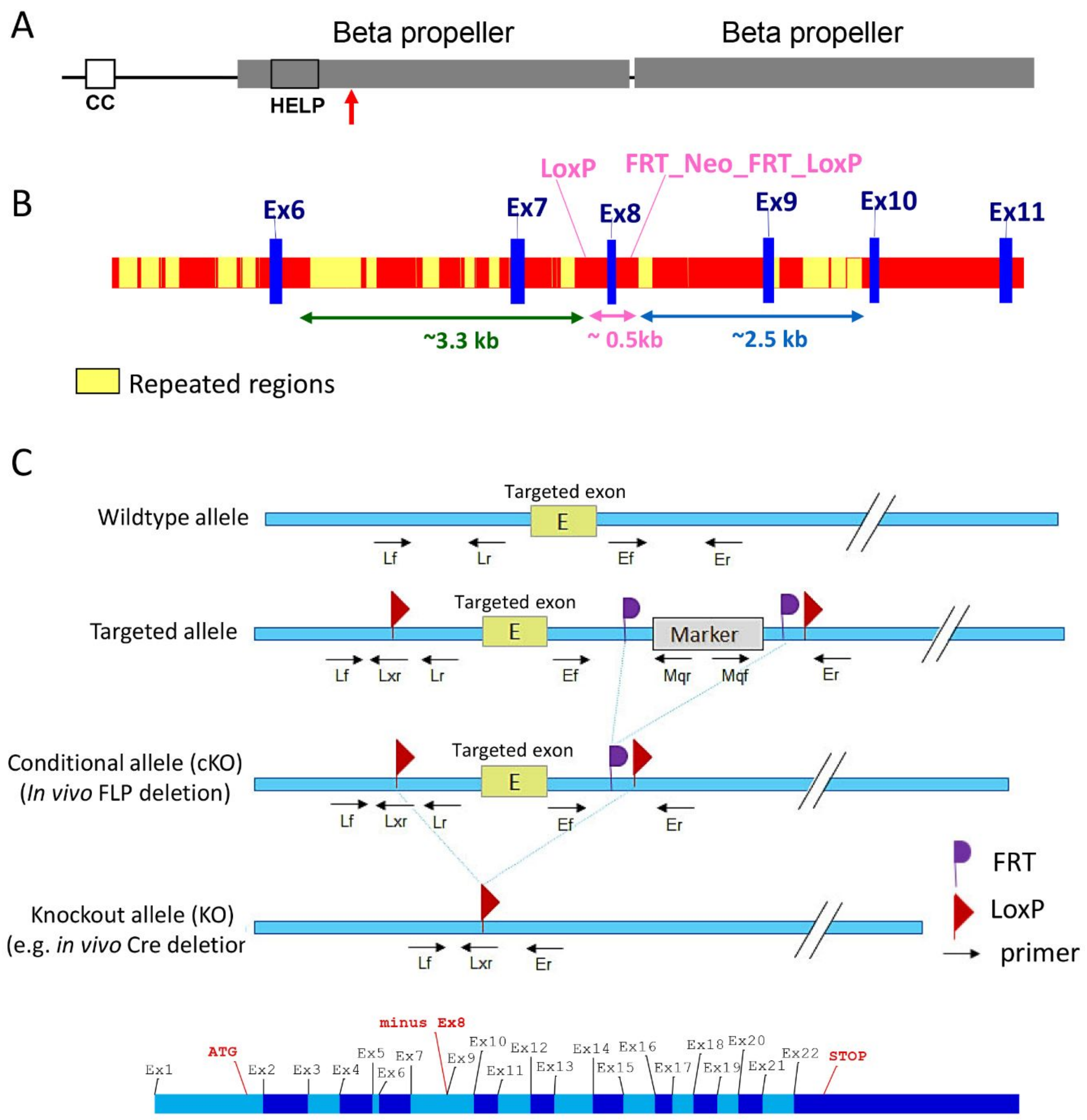

Supplementary Figure 1 *Eml*1 KO strategy. (A) Schematic of Eml1 protein domains, CC, coiled coil motif, HELP, hydrophobic EMAP-Like Protein motif. **(B)** Gene region showing modifications introduced in the targeting construct surrounding exon 8. **(C)** Schematic showing primers surrounding targeted exon 8 (‘E’), red triangles indicate loxP sites and purple flags indicate FRT sites. Marker indicates Neo cassette. Mice carrying the knockout allele were produced showing a deletion of exon 8 (70 bp), leading to a frameshift and premature stop codon when exon 7 is spliced to exon 9.

For Peer Review Only

Supplementary Figure 2

Adult screen Lateral +0.60mm (right hemisphere)

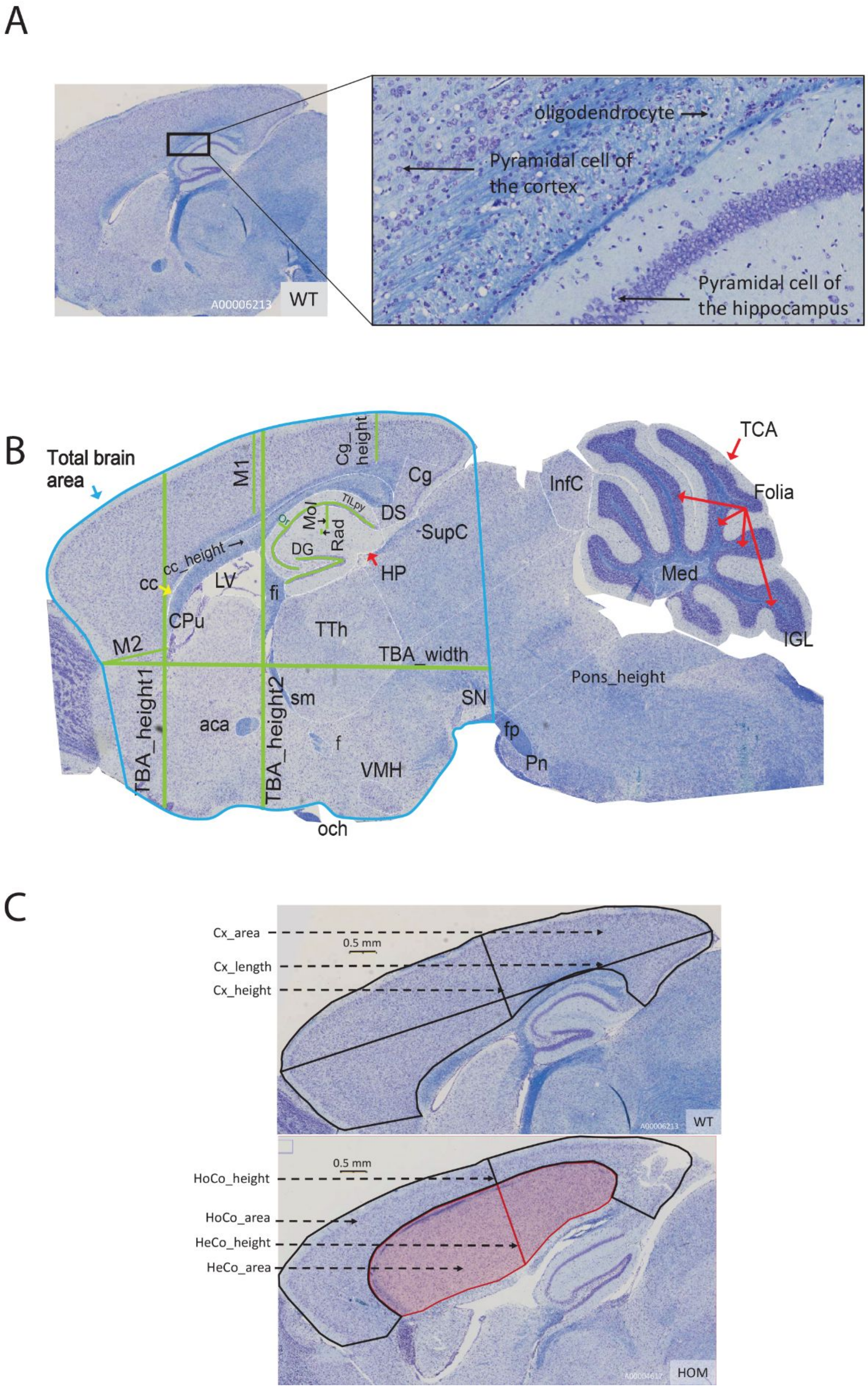

Supplementary Figure 2. Adult screen. Resolution and adult mouse brain atlas. (**A**) Zoomed image of a WT animal at 7 weeks of age. (**B**) Adult mouse brain atlas at Lateral 600 μm (right hemisphere). A full description of the acronyms used in this Figure is provided in **Supp. Table 1**. (**C**) Additional 7 parameters added to the initial screen in order to further characterize the subcortical band heterotopia in *Eml*1$^{-/-}$ mice.

For Peer Review Only

Supplementary Figure 3

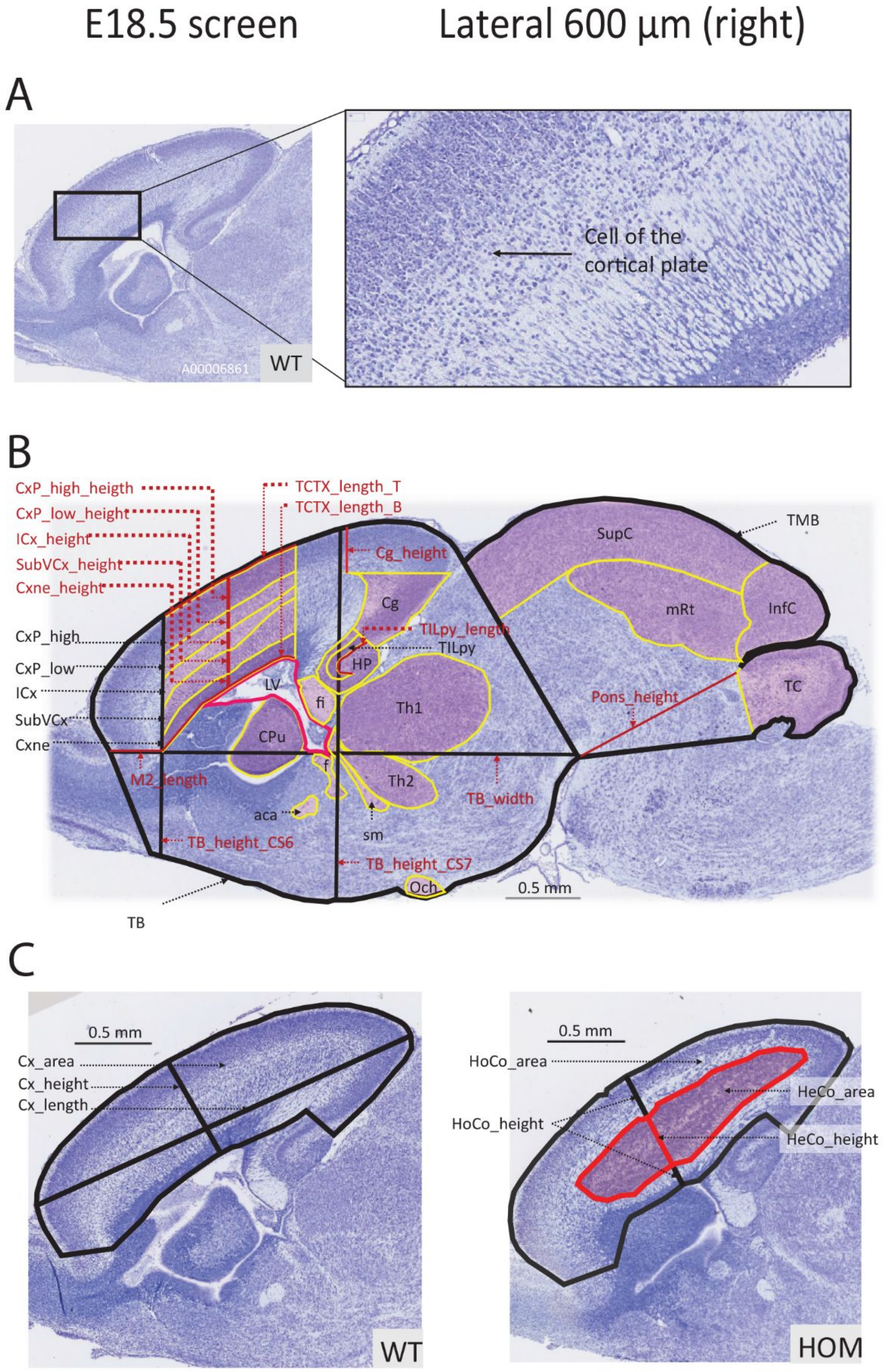

Supplementary Figure 3. Embryonic screen (E18.5). Resolution and E18.5 mouse brain atlas. (**A**) Zoomed image of a WT animal at E18.5. (**B**) E18.5 mouse brain atlas of 39 parameters at Lateral 600 μm (right hemisphere). Red font indicates length and black font area measurements. (**C**) Additional 7 parameters added to the initial screen in order to further characterize the subcortical band heterotopia in *Eml*$1^{-/-}$ mice.

For Peer Review Only

Supplementary Figure 4

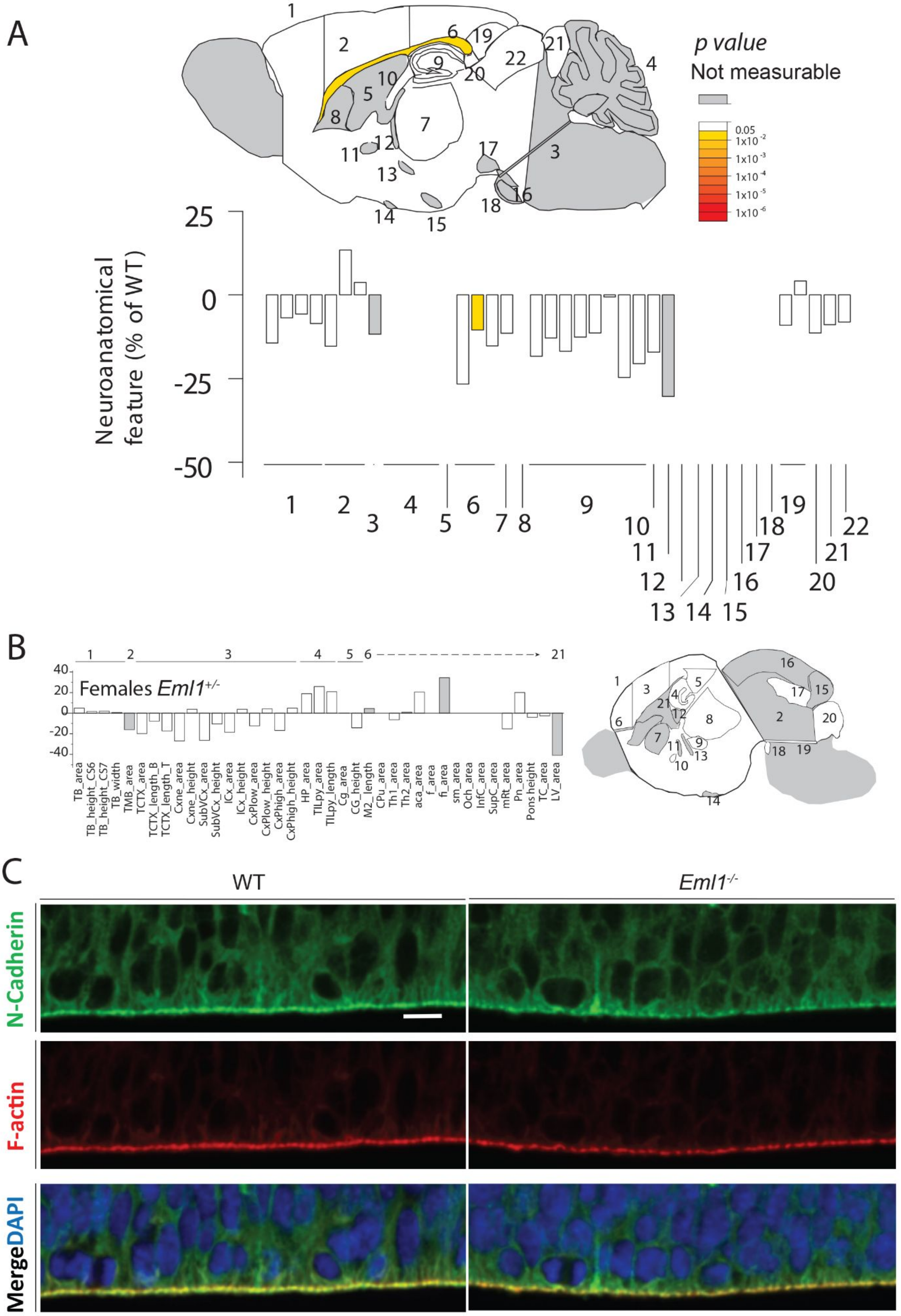

Supplementary Figure 4. Schematic representation of brain regions in *Eml*1$^{+/-}$ female mice at P13 (A) and E18.5 (B). *Eml*1 KO mice do not show major disruptions in the adherens junctions - actin belt at E13.5 (C). Representative images of immunohistochemistry performed in WT and hom mice for N-Cadherin (green), F-actin (red) and Hoechst (blue). Scale bar 10 µm.

For Peer Review Only

Supplementary Table 1

Parameter	Description
4_TB_area	Total brain area
4_TC_area	Total cerebellar area
4_LV_area	Lateral ventricle area
4_cc_area	Corpus callosum area
4_cc_cellcount	Cell count of the corpus callosum
4_cc_cellarea	Total cell area of the corpus callosum
4_cc_celldens	Cell density of the corpus callosum
4_cc_avgcellarea	Average cell area of the corpus callosum
4_cc_cellcirc	Cell circularity of the corpus callosum
4_cc_cellsol	Cell solidity of the corpus callosum
4_TCTX_area	Total cortical area
4_TCTX_cellcount	Cell count of the cortex
4_TCTX_cellarea	Total cell area of the cortex
4_TCTX_celldens	Cell density of the cortex
4_TCTX_avgcellarea	Average cell area of the cortex
4_TCTX_cellcirc	Cell circularity of the cortex
4_TCTX_cellsol	Cell solidity of the cortex
4_TTh_area	Total thalamic area
4_TTh_cellcount	Cell count of the thalamus
4_TTh_cellarea	Total cell area of the thalamus
4_TTh_celldens	Cell density of the thalamus
4_TTh_avgcellarea	Average cell area of the thalamus
4_TTh_cellcirc	Cell circularity of the thalamus
4_TTh_cellsol	Cell solidity of the thalamus
4_CPu_area	Caudate putamen area
4_CPu_cellcount	Cell count of the caudate putamen
4_CPu_cellarea	Total cell area of the caudate putamen
4_CPu_celldens	Cell density of the caudate putamen
4_CPu_avgcellarea	Average cell area of the caudate putamen
4_CPu_cellcirc	Cell circularity of the caudate putamen
4_CPu_cellsol	Cell solidity of the caudate putamen
4_HP_area	Hippocampus area
4_HP_cellcount	Cell count of the hippocampus
4_HP_cellarea	Total cell area of the hippocampus
4_HP_celldens	Cell density of the hippocampus
4_HP_avgcellarea	Average cell area of the hippocampus
4_HP_cellcirc	Cell circularity of the hippocampus
4_HP_cellsol	Cell solidity of the hippocampus
4_TILpy_area	Area of pyramidal cells of the hippocampus
4_TILpy_cellcount	Cell count of the pyramidal cells of the hippocampus
4_TILpy_cellarea	Total cell area of the pyramidal cells of the hippocampus
4_TILpy_celldens	Cell density of the pyramidal cells of the hippocampus
4_TILpy_avgcellarea	Average cell area of the pyramidal cells of the hippocampus

For Peer Review Only

4_TILpy_cellcirc	Cell circularity of the pyramidal cells of the hippocampus
4_TILpy_cellsol	Cell solidity of the pyramidal cells of the hippocampus
4_DG_area	Dentate gyrus area
4_DG_cellcount	Cell count of the dentate gyrus
4_DG_cellarea	Total cell area of the dentate gyrus
4_DG_celldens	Cell density of the dentate gyrus
4_DG_avgcellarea	Average cell area of the dentate gyrus
4_DG_cellcirc	Cell circularity of the dentate gyrus
4_DG_cellsol	Cell solidity of the dentate gyrus
4_fi_area	Area of the fimbria of the hippocampus
4_fi_cellcount	Cell count of the fimbria of the hippocampus
4_fi_cellarea	Total cell area of the fimbria of the hippocampus
4_fi_celldens	Cell density of the fimbria of the hippocampus
4_fi_avgcellarea	Average cell area of the fimbria of the hippocampus
4_fi_cellcirc	Cell circularity of the fimbria of the hippocampus
4_fi_cellsol	Cell solidity of the fimbria of the hippocampus
4_aca_area	Anterior commissure area
4_aca_cellcount	Cell count of the anterior commissure
4_aca_cellarea	Total cell area of the anterior commissure
4_aca_celldens	Cell density of the anterior commissure
4_aca_avgcellarea	Average cell area of the anterior commissure
4_aca_cellcirc	Cell circularity of the anterior commissure
4_aca_cellsol	Cell solidity of the anterior commissure
4_sm_area	Stria medullaris area
4_sm_cellcount	Cell count of the stria medullaris
4_sm_cellarea	Total cell area of the stria medullaris
4_sm_celldens	Cell density of the stria medullaris
4_sm_avgcellarea	Average cell area of the stria medullaris
4_sm_cellcirc	Cell circularity of the stria medullaris
4_sm_cellsol	Cell solidity of the stria medullaris
4_f_area	Fornix area
4_f_cellcount	Cell count of the fornix
4_f_cellarea	Total cell area of the fornix
4_f_celldens	Cell density of the fornix
4_f_avgcellarea	Average cell area of the fornix
4_f_cellcirc	Cell circularity of the fornix
4_f_cellsol	Cell solidity of the fornix
4_och_area	Optic chiasm area
4_och_cellcount	Cell count of the optic chiasm
4_och_cellarea	Total cell area of the optic chiasm
4_och_celldens	Cell density of the optic chiasm
4_och_avgcellarea	Average cell area of the optic chiasm
4_och_cellcirc	Cell circularity of the optic chiasm
4_och_cellsol	Cell solidity of the optic chiasm
4_VMHvl_area	Area of ventromedial nucleus of the hypothalamus

For Peer Review Only

4_VMHvl_cellcount	Cell count of the ventromedial nucleus of the hypothalamus
4_VMHvl_cellarea	Total cell area of the ventromedial nucleus of the hypothalamus
4_VMHvl_celldens	Cell density of the ventromedial nucleus of the hypothalamus
4_VMHvl_avgcellarea	Average cell area of the ventromedial nucleus of the
4_VMHvl_cellcirc	Cell circularity of the ventromedial nucleus of the hypothalamus
4_VMHvl_cellsol	Cell solidity of the ventromedial nucleus of the hypothalamus
4_Pn_area	Pontine nuclei area
4_Pn_cellcount	Cell count of the pontine nuclei
4_Pn_cellarea	Total cell area of the pontine nuclei
4_Pn_celldens	Cell density of the pontine nuclei
4_Pn_avgcellarea	Average cell area of the pontine nuclei
4_Pn_cellcirc	Cell circularity of the pontine nuclei
4_Pn_cellsol	Cell solidity of the pontine nuclei
4_SN_area	Substantia nigra area
4_SN_cellcount	Cell count of the substantia nigra
4_SN_cellarea	Total cell area of the substantia nigra
4_SN_celldens	Cell density of the substantia nigra
4_SN_avgcellarea	Average cell area of the substantia nigra
4_SN_cellcirc	Cell circularity of the substantia nigra
4_SN_cellsol	Cell solidity of the substantia nigra
4_fp_area	Area of fibre of pons
4_fp_cellcount	Cell count of the fibre of pons
4_fp_cellarea	Total cell area of the fibre of pons
4_fp_celldens	Cell density of the fibre of pons
4_fp_avgcellarea	Average cell area of the fibre of pons
4_fp_cellcirc	Cell circularity of the fibre of pons
4_fp_cellsol	Cell solidity of the fibre of pons
4_Cg_area	Cingulate cortex area
4_Cg_cellcount	Cell count of the cingulate cortex
4_Cg_cellarea	Total cell area of the cingulate cortex
4_Cg_celldens	Cell density of the cingulate cortex
4_Cg_avgcellarea	Average cell area of the cingulate cortex
4_Cg_cellcirc	Cell circularity of the cingulate cortex
4_Cg_cellsol	Cell solidity of the cingulate cortex
4_DS_area	Dorsal subiculum area
4_DS_cellcount	Cell count of the dorsal subiculum
4_DS_cellarea	Total cell area of the dorsal subiculum
4_DS_celldens	Cell density of the dorsal subiculum
4_DS_avgcellarea	Average cell area of the dorsal subiculum
4_DS_cellcirc	Cell circularity of the dorsal subiculum
4_DS_cellsol	Cell solidity of the dorsal subiculum
4_InfC_area	Inferior colliculus area
4_InfC_cellcount	Cell count of the inferior colliculus
4_InfC_cellarea	Total cell area of the inferior colliculus

For Peer Review Only

4_InfC_celldens	Cell density of the inferior colliculus
4_InfC_avgcellarea	Average cell area of the inferior colliculus
4_InfC_cellcirc	Cell circularity of the inferior colliculus
4_InfC_cellsol	Cell solidity of the inferior colliculus
4_SupC_area	Superior colliculus area
4_SupC_cellcount	Cell count of the superior colliculus
4_SupC_cellarea	Total cell area of the superior colliculus
4_SupC_celldens	Cell density of the superior colliculus
4_SupC_avgcellarea	Average cell area of the superior colliculus
4_SupC_cellcirc	Cell circularity of the superior colliculus
4_SupC_cellsol	Cell solidity of the superior colliculus
4_Med_area	Area of the medial cerebellar nucleus
4_Med_cellcount	Cell count of the medial cerebellar nucleus
4_Med_cellarea	Total cell area of the medial cerebellar nucleus
4_Med_celldens	Cell density of the medial cerebellar nucleus
4_Med_avgcellarea	Average cell area of the medial cerebellar nucleus
4_Med_cellcirc	Cell circularity of the medial cerebellar nucleus
4_Med_cellsol	Cell solidity of the medial cerebellar nucleus
4_TILpy_length	Total internal length of pyramidal cell layer of the hippocampus
4_DG_length	Dentate gyrus length
4_cc_length	Total outer length of the corpus callosum
4_Mol_length	Length of the molecular layer of the hippocampus
4_Rad_length	Length of the radiatum layer of the hippocampus
4_Or_length	Length of the oriens layer of the hippocampus
4_cc_height	Corpus callosum thickness
4_M2_length	Length of the secondary motor cortex
4_M1_length	Length of the primary motor cortex
4_Cg_height	Height of the cingulate cortex
4_TB_width	Width of the total brain
4_TB_height_CS1	Height of the total brain at CS1 (coronal critical section 1)
4_TB_height_CS2	Height of the total brain at CS2 (coronal critical section 2)
4_Pons_height	Height of the pons
4_IGL_area	Area of the internal granular layer of the cerebellum
4_Folia	Number of folia

For Peer Review Only

Unit
cm2
cm2
cm2
cm2
digit
cm2
digit
cm2
digit
digit
cm2
digit
cm2
digit
cm2
digit
digit
cm2
digit
cm2
digit
cm2
digit
digit
cm2
digit
cm2
digit
cm2
digit
digit
cm2
digit
cm2
digit
cm2
digit
digit
cm2
digit
cm2
digit
cm2

For Peer Review Only

digit
digit
cm2
digit
cm2
digit
cm2
digit
digit
cm2
digit
cm2
digit
cm2
digit
digit
cm2
digit
cm2
digit
cm2
digit
digit
cm2
digit
cm2
digit
cm2
digit
digit
cm2
digit
cm2
digit
cm2
digit
digit
cm2
digit
cm2
digit
cm2
digit
digit
cm2

For Peer Review Only

digit
cm2
digit
cm2
digit
digit
cm2
digit
cm2
digit
cm2
digit
digit
cm2
digit
cm2
digit
cm2
digit
digit
cm2
digit
cm2
digit
cm2
digit
digit
cm2
digit
cm2
digit
cm2
digit
digit
cm2
digit
cm2
digit
cm2
digit
digit
cm2
digit
cm2

For Peer Review Only

digit
cm2
digit
digit
cm2
digit
cm2
digit
cm2
digit
digit
cm2
digit
cm2
digit
cm2
digit
digit
cm
cm
cm
cm
cm
cm
cm
cm
cm
cm
cm
cm
cm
cm
cm2
digit

For Peer Review Only

Supplementary Table 2

Analysis	Critical_section
Sagittal Sections E18.5	Sagittal (Lateral 0.6 mm, right)

For Peer Review Only

Brain_region	Parameter
Forebrain	9_TB_area
Forebrain	9_TB_height_CS6
Forebrain	9_TB_height_CS7
Forebrain	9_TB_width
Cortex	9_TCTX_area
Cortex	9_TCTX_length_B
Cortex	9_TCTX_length_T
Cortex	9_Cxne_area
Cortex	9_Cxne_height
Cortex	9_SubVCx_area
Cortex	9_SubVCx_height
Cortex	9_ICx_area
Cortex	9_ICx_height
Cortex	9_CxP_low_area
Cortex	9_CxP_low_height
Cortex	9_CxP_high_area
Cortex	9_CxP_high_height
Cortex	9_M2_ length
Hippocampus	9_HP_area
Hippocampus	9_TILpy_area
Hippocampus	9_TILpy_length
Cortex	9_Cg_area
Cortex	9_Cg_height
Ventricle	9_LV_area
Basal Ganglia	9_CPu_area
Thalamus	9_Th1_area
Thalamus	9_Th2_area
Fiber tract	9_fi_area
Fiber tract	9_aca_area
Fiber tract	9_f_area
Fiber tract	9_sm_area
Fiber tract	9_Och_area
Midbrain	9_TMB_area
Midbrain	9_InfC_area
Midbrain	9_SupC_area
Midbrain	9_mRt_area
Cerebellum	9_TC_area
Pons	9_Pn_area
Pons	9_Pons height

For Peer Review Only

Description
Total brain area, forebrain
Total brain height, forebrain, corresponding to critical section 6
Total brain height, forebrain, corresponding to critical section 7
Total brain width, forebrain
Total cortical area of the future secondary motor cortex
Total cortical length (Bottom)
Total cortical length (Top)
Neuroepithelial cortex area
Neuroepithelial cortex height
Subventricular cortex area
Subventricular cortex height
Intermediate cortex area
Intermediate cortex height
Cortical plate lower area
Cortical plate lower height
Cortical plate higher area
Cortical plate higher height
Secondary motor cortex length
Hippocampus area
Total internal layer of pyramidal cells area
Total internal layer of pyramidal cells length
Cingulate cortex height
Cingulate cortex area
Lateral ventricle area
Caudate-Putamen area
Thalamus area 1
Thalamus area 2
Fimbria area
Anterior commissure area
Fornix area
Stria medullaris area
Optic chiasm area
Total midbrain area
Inferior colliculus area
Superior colliculus area
Mesencephalic reticular formation area
Total cerebellum area
Pontine nucleus area
Pons height

For Peer Review Only

Category	**Unit**
Area	cm²
Length	cm
Length	cm
Length	cm
Area	cm²
Length	cm
Length	cm
Area	cm²
Length	cm
Area	cm²
Length	cm
Area	cm²
Length	cm
Area	cm²
Length	cm
Area	cm²
Length	cm
Length	cm
Area	cm²
Area	cm²
Length	cm
Area	cm²
Length	cm
Area	cm²
Area	cm²
Area	cm²
Area	cm²
Area	cm²
Area	cm²
Area	cm²
Area	cm²
Area	cm²
Area	cm²
Area	cm²
Area	cm²
Area	cm²
Area	cm²
Area	cm²
Length	cm

For Peer Review Only

For Peer Review Only